

LightSplit: Practical Privacy-Preserving Split Learning via Orthogonal Projections

Mert Cihangiroglu¹, Alessandro Pegoraro², Phillip Rieger², Antonino Nocera¹, Ahmad-Reza Sadeghi²
¹University of Pavia ²Technical University of Darmstadt

Abstract—Split learning (SL) enables collaborative training by partitioning a neural network across clients and a central server, but the cut-layer interface introduces a key challenge: high-dimensional activations incur substantial communication overhead while exposing representations vulnerable to reconstruction attacks. Existing approaches typically address efficiency or privacy in isolation, relying on additional mechanisms such as sparsification, quantization, or noise injection.

We propose LIGHTSPLIT, which limits information exposure and reduces communication overhead by applying a lightweight fixed orthogonal random projection at the cut layer. Based on Shannon’s information theory, this projection acts as an information bottleneck that restricts instance-specific information and suppresses exploitable per-sample signals. By transmitting low-dimensional projections instead of raw activations, the server operates on lifted representations without requiring architectural modifications, ensuring compatibility with existing SL architectures. By avoiding additional trainable components on the client, the method remains lightweight and suitable for edge devices while preserving end-to-end differentiability via exact gradient propagation. As the projection is non-invertible, part of the original representation is irreversibly discarded at the client, LightSplit reduces the information available for reconstruction and limits information exposure.

We extensively evaluate LIGHTSPLIT on state-of-the-art benchmarks in both IID and non-IID settings across varying projection dimensions and client scales. Our results show that the method retains more than 95% of the baseline accuracy at up to 32× reduction in transmitted dimensionality while maintaining stable training dynamics.

I. INTRODUCTION

Split learning (SL) enables computationally restricted devices to perform training and inference of deep neural networks (DNNs) without sharing their potentially sensitive data. Instead of outsourcing the entire process to a powerful server, the DNN is split into multiple fragments, the head and the backbone. The first layers of the DNN process sensitive input data, form the head, and are located and processed on the local device. The activations of the final layer of the head, which are known as smashed data, are then sent to the server, and the server completes the forward and backward passes through the remaining layers, which form the backbone [41], [19]. Sharing the server located backbone enables clients to benefit from each others’ data without sharing them. Unlike Federated Learning (FL) [33], in which the client is required to provide sufficient resources to hold a full model copy, SL is also suitable for edge scenarios where devices possess limited memory and computing resources.

Communication Overhead and Privacy Attacks. The convenience comes at two costs. First, the smashed data must be

exchanged at every training step, creating a communication bottleneck that scales linearly with the activation dimensionality. For a standard ResNet-18 [21], this amounts to over 150GB of network traffic for a training run on a modest CIFAR-10 with five clients (Table I). Second, the smashed data is an information-rich intermediate representation that an honest-but-curious server can exploit. Indeed, many novel works have shown that SL is susceptible to multiple security threats, such as input reconstruction [9], [47], [56], label leakage [29], and backdoor manipulation [50]. In particular, server-based reconstruction attacks pose a critical risk (notably SDAR [56]), demonstrating that a passive server can recover client inputs from uncompressed, smashed data with high fidelity, undermining the privacy premise of SL. In this work, we focus on mitigating such threats and protecting client data under these adversarial conditions.

Existing Literature. Prior work in the cut layer addresses privacy or communication efficiency in isolation. Privacy-focused defenses [42], [34], [38] perturb activations to resist reconstruction, but transmit them at full dimensionality and leave the communication bottleneck untouched. Communication efficiency focused methods reduce payload via compression, but each comes with its own limitations: top- k sparsification and its variants [53], [54] reveal which positions are most active per input, learned codecs [37], [13] require trainable encoders and external pretraining on the client, and batch-wise compression [23] reduces transmissions per round but not the per-sample payload. Cryptographic mechanisms [30], [17] provide formal confidentiality at orders-of-magnitude computational overhead, which is unsuitable for resource-constrained clients. To our knowledge, no existing method simultaneously reduces the per-sample payload, avoids client-side overhead, and limits the information exposed to the server under a semi-honest threat model.

Goals and Contributions. To address both privacy leakage and communication overhead in split learning, we introduce LIGHTSPLIT. The method projects cut-layer activations into a lower-dimensional subspace using a lightweight orthogonal transformation inspired by the Johnson-Lindenstrauss (JL) lemma [24]. This projection reduces the amount of transmitted data while constraining instance-specific information that can be exploited by reconstruction attacks. To further limit residual leakage, the training process reduces intra-class variation in the transmitted representations, encouraging samples of the same class to form compact clusters. As a result, the representation behaves more like a class prototype than an instance-specific

TABLE I: Aggregate split-point communication cost over 100 epochs for $N=5$ clients on CIFAR-10.

Compression ρ	Payload k	Floats/sample	Total (GB)	
(Raw)	$1\times$	4,096	8,192	152.6
	$8\times$	512	1,024	19.1
	$16\times$	256	512	9.5
	$32\times$	128	256	4.8

descriptor, making individual samples harder to distinguish. Together, these components allow LIGHTSPLIT to limit information exposure while maintaining model utility and to seamlessly integrate into existing SL architectures without requiring modifications to the underlying network. The fixed projection and the regularization jointly allow the client model to align its representations with the projected subspace, enabling co-adaptation to the reduced interface without increasing the complexity of the bottleneck. Our contributions include:

- We introduce LIGHTSPLIT, a split learning framework that jointly addresses communication overhead and privacy leakage. By projecting smashed data into a fixed, randomly chosen orthonormal subspace, LightSplit discards information in the orthogonal complement, limiting the information available for reconstruction attacks and thereby mitigating privacy leakage.
- We design an irreversible information bottleneck through the projection that discards components orthogonal to the projected subspace, limits information accessible to a curious server and degrades reconstruction attacks by making the inverse mapping underdetermined (Sect. IV-B).
- We design a Within-Class Compaction (WCC) regularizer that preserves model utility by encouraging the client model to align its representations with the surviving subspace. Thus, LightSplit enables the client to retain task-relevant information and maintain competitive accuracy even under non-IID data distributions (Sect. IV-D).
- LIGHTSPLIT introduces negligible overhead by employing a fixed orthonormal projection on the client, requiring only a single matrix multiplication without additional learnable parameters. On the server side, it supports two lift-back modes allowing us to trade off flexibility and computational efficiency, enabling operation without any additional learnable parameters (Sect. IV-C).
- As a consequence of suppressing task-irrelevant variation while preserving class-discriminative features, the projections emphasize class-level structure. This improves separability in the projected space and can benefit analysis tasks that rely on robust feature representations, including server-side detection mechanisms (Sect. V-B4).
- We perform a comprehensive evaluation across multiple architectures and datasets, demonstrating that LIGHTSPLIT reduces reconstruction capability of state-of-the-art attacks up to $7\times$ and reduces communication overhead up to $32\times$ while retaining 97.3% of the original accuracy (Sect. V).

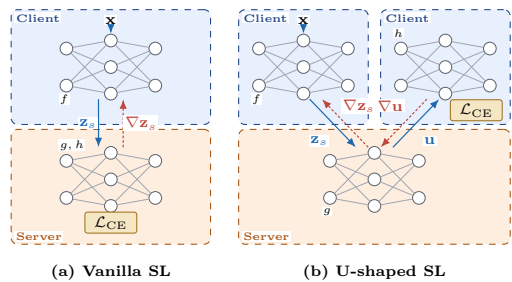


Fig. 1: Vanilla and U-shaped split-learning topologies.

II. BACKGROUND

A. Split Learning

In split learning (SL) [19], a DNN is partitioned at a designated *cut layer* between a client holding privacy-sensitive data and a server with strong computational resources. In the simplest configuration (vanilla), the client holds the first layers f , and the server holds the remainder g , including the classifier. Therefore, the server has access to both the intermediate activations and the training labels, as visualized in Fig. 1a. In the *U-shaped* configuration [41], the model is split into three parts $H = h \circ g \circ f$: the client holds both the head f (early layers) and the tail h , while the server holds only the intermediate backbone g , as visualized in Fig. 1b. We adopt U-shaped SL throughout this work, as it represents a more realistic and challenging setting: labels are private by design, and the server must reconstruct without access to them.

During each training step, the client feeds its private input \mathbf{x} through f to produce the intermediate activation tensor, termed *smashed data*, and transmits it to the server. For a ResNet-18 [21] head on 32×32 CIFAR-10 [27] inputs, this produces a $64 \times 8 \times 8$ feature map ($d = 4,096$ scalar values once flattened). The server runs the backbone g and returns its output to the client, where the tail h produces the final prediction and evaluates the task loss. Gradients flow back through the same path: the client calculates the loss and backpropagates through h , passes the gradient to the server for backpropagation through g , and receives $\nabla_{\mathbf{z}}\mathcal{L}$ to update f . Because both raw data and labels remain on the client, the server observes only the intermediate activations and the corresponding gradients, but never inputs, labels, or the final loss. In multi-client settings [40], communication scales with both the cut-layer width d and the number of participating clients [45], [44]: every round requires transmitting a d -dimensional activation *and* a d -dimensional gradient per client per batch, as illustrated in Tab. I. Note that SL differs from federated learning [33] in that there is no local model copy or periodic aggregation. All clients contribute to the same shared backbone through sequential gradient updates. However, there is a collaborative version of SL, where clients exchange the weights and biases of the head and tail, enabling other clients to benefit from their training.

B. Random Projections and Johnson-Lindenstrauss Lemma

The Johnson-Lindenstrauss (JL) lemma [24] states that a random linear map $\mathbf{R} \in \mathbb{R}^{d \times k}$ with orthonormal columns preserves pairwise Euclidean distances among a finite point set up to a $(1 \pm \varepsilon)$ factor with high probability, provided $k = \Omega(\varepsilon^{-2} \log n)$. For any two activations $\mathbf{h}_i, \mathbf{h}_j \in \mathbb{R}^d$, the projected pair satisfies:

$$(1-\varepsilon)\|\mathbf{h}_i - \mathbf{h}_j\|^2 \leq \|\mathbf{R}^\top \mathbf{h}_i - \mathbf{R}^\top \mathbf{h}_j\|^2 \leq (1+\varepsilon)\|\mathbf{h}_i - \mathbf{h}_j\|^2. \quad (1)$$

Applied to cut-layer activations, this implies that the geometric structure underlying class separability, inter-class distances and intra-class clustering, is preserved under \mathbf{R} without any task-adaptive optimization.

Dimensionality reduction does not automatically guarantee privacy. Blocki et al. [3] and Kenthapadi et al. [25] show that formal privacy guarantees for JL-style transforms require added noise and single-shot release, conditions that do not hold under repeated or auxiliary-informed observation, precisely the conditions of iterative SL training. Bora et al. [4] prove that signals near the range of a generative model can be recovered from as few as $O(k_{\text{gen}} \log d)$ measurements, far fewer than the ambient dimension. As we will elaborate in Sect. IV-D, LightSplit builds on the JL-lemma but complements it with a within-class regularizer to guide training towards class prototypes and to remove instance descriptions that may leak information. The absence of formal privacy guarantees of the JL-lemma motivates our decision to evaluate privacy *empirically* under adaptive attackers rather than relying on dimensionality reduction as an implicit guarantee.

III. PROBLEM SETTING

A. System Model

We study the U-shaped SL (see Sect. II-A) where n clients share a server-side backbone g , each client holds head f and tail h , and the cut-layer activation $\mathbf{z} = f(\mathbf{x}) \in \mathbb{R}^d$ is the sole object transmitted. Every training step requires sending a d -dimensional activation *and* receiving a d -dimensional gradient per sample, so aggregate bandwidth scales linearly with d and the number of clients. Our goal is to replace the transmitted \mathbf{z} with a k -dimensional summary ($k \ll d$) that preserves task utility while restructuring what the server observes.

B. Threat Model

In the following, we consider an adversary that aims to infer information about the clients' samples, i.e., reconstruct them.

We adopt the *honest-but-curious* (semi-honest) threat model: the server faithfully executes the training protocol but may attempt to infer clients' private data from the information it legitimately receives. During training, the server observes the compressed activations $\tilde{\mathbf{z}}_i \in \mathbb{R}^k$ (not the original $\mathbf{z}_i \in \mathbb{R}^d$), the gradients $\nabla \tilde{\mathbf{z}}_i$ returned to clients, and its own backbone parameters θ_g , which evolve throughout training.

C. Requirements and Challenges

An approach that effectively addresses and is practical needs to fulfill the following requirements:

R1 - Attack Prevention: The method must prevent or significantly deter reconstruction and inference attacks of curious servers, under the assumed threat model.

R2 - Model Utility Preservation: In order to be practical, the approach must maintain model performance comparable to the uncompressed baseline, avoiding degradation in task accuracy or convergence stability.

R3 - Communication Efficiency: The method must reduce the dimensionality of transmitted representations, thereby lowering communication overhead at the cut layer, which dominates the overall training cost.

Projecting cut-layer activations and addressing privacy leakage while maintaining utility is fundamentally different from standard model compression or gradient quantization. Therefore, methods that meet these requirements must overcome several research challenges.

C1 - Shared backbone constrains unilateral compression:

A first challenge arises from the shared server-side backbone g , which prevents clients from independently applying arbitrary compression to their smashed data. Since g is trained on the received representations, uncoordinated compression induces distribution shifts, producing out-of-distribution inputs that destabilize the backbone across clients. Thus, compression cannot be a purely local design choice but must follow a globally consistent protocol. A challenge is therefore how to ensure compatibility across clients and preserve a shared representation space while maintaining compression efficiency, a constraint that becomes even more critical in SL variants with individual client heads.

C2 - Compression and privacy are entangled:

A second challenge arises from the inherent tension between compression and privacy. Naïve compression approaches aim to preserve as much information as possible, which directly conflicts with the goal of limiting information leakage. In particular, retaining the most informative components often preserves exactly the signal exploited by reconstruction attacks. For instance, Top- K sparsification [53], [54] reveals *which* neurons fire most for each input, effectively exposing a per-sample feature saliency map. Similarly, learned codecs [37], [13] are explicitly optimized for high-fidelity reconstruction of activations, which directly opposes the objective of limiting what the server can recover about the input. A challenge is therefore how to design compression mechanisms that retain task-relevant structure, specifically inter-class geometry, while discarding the per-sample variation that enables reconstruction.

C3 - Client overhead undermines the SL premise:

A third challenge arises from the resource constraints of clients in SL. Any compression mechanism that introduces additional trainable components increases the very cost that SL is designed to minimize. At the same time, fixed, non-trainable compression must produce task-compatible representations without adapting to the data distribution. A challenge is therefore, how

to design lightweight compression mechanisms that preserve utility without increasing client-side complexity.

IV. LIGHTSPLIT

To improve privacy and communication efficiency in SL and address the aforementioned challenges, we introduce LightSplit, which projects smashed data into a lower-dimensional subspace to reduce communication and limit information exposure.

A. Design Rationale

To reduce information exposure and mitigate reconstruction attacks while improving communication efficiency, LightSplit projects smashed data into a lower-dimensional subspace and lets the server operate on reconstructed, back-lifted representations. Privacy attacks typically exploit subtle, instance-specific variations in the transmitted activations. The core challenge is therefore to preserve task-relevant, discriminative features while suppressing information that enables reconstruction.

LightSplit employs a projection that builds on the Johnson-Lindenstrauss (JL) lemma (see Sect. II-B), which guarantees that pairwise distances are approximately preserved under random projection. This ensures that class structure and separability remain intact despite dimensionality reduction. Concretely, each client applies a fixed orthonormal projection matrix $\mathbf{R} \in \mathbb{R}^{d \times k}$ to map smashed activations $\mathbf{z} \in \mathbb{R}^d$ (cut-layer dimension d) to projected representations $\tilde{\mathbf{z}} = \mathbf{R}^\top \mathbf{z} \in \mathbb{R}^k$ (projected dimension k , with $k \ll d$).

On the server side, we introduce two variants for processing the projected activations: LIGHTSPLIT-F and LIGHTSPLIT-L. LIGHTSPLIT-F uses a fixed linear lift-back mapping, while LIGHTSPLIT-L employs a trainable network to reconstruct task-compatible representations. The fixed variant is parameter-free and computationally lightweight, whereas the learned variant increases flexibility and can better adapt to the projected representation.

After server-side processing, the client receives the intermediate output, completes the forward pass via the tail, and computes the task loss \mathcal{L}_{CE} . In addition, we introduce a Within-Class Compaction (WCC) loss that reduces intra-class variation in the transmitted representations. This discourages instance-specific feature scattering that can be exploited by reconstruction attacks, while preserving class-level structure necessary for accurate prediction.

B. Client-Side Projection

A client-side projection in SL must reduce the cut-layer payload while addressing the resource constraints of devices that restrict introducing additional trainable components in some scenarios. At the same time, it should limit the amount of per-sample information exposed to the server. LightSplit solves these challenges through the design of a fixed random projection at the cut layer.

Each client projects its smashed activation $\mathbf{z} \in \mathbb{R}^d$ into a lower-dimensional representation $\tilde{\mathbf{z}} \in \mathbb{R}^k$ using a fixed orthonormal matrix $\mathbf{R} \in \mathbb{R}^{d \times k}$:

$$\mathbf{R}^\top: \mathbb{R}^d \rightarrow \mathbb{R}^k, \quad \mathbf{z} \mapsto \tilde{\mathbf{z}} = \mathbf{R}^\top \mathbf{z}, \quad k \ll d. \quad (2)$$

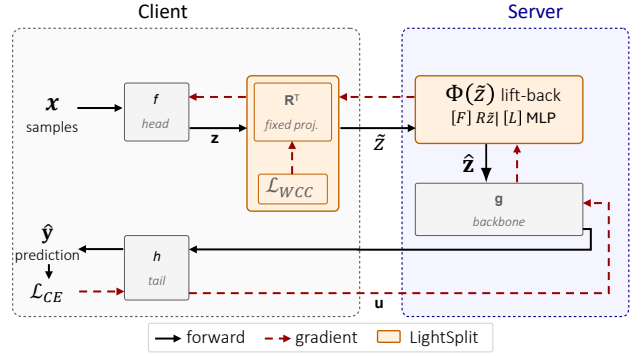


Fig. 2: Overview of LightSplit for U-shaped SL setup with client-located head f and tail h , and server-side backbone g . LightSplit components are highlighted by orange boxes. Inputs \mathbf{x} are mapped to activation \mathbf{z} , which are projected to representations $\tilde{\mathbf{z}} \in \mathbb{R}^k$ before transmission. The server reconstructs activations as $\hat{\mathbf{z}}$ via lift-back function ϕ and processes by g , obtaining smashed data \mathbf{u} . Client computes the prediction \hat{y} and task loss \mathcal{L}_{CE} and WCC loss \mathcal{L}_{WCC} .

The matrix \mathbf{R} is broadcast in the beginning to all clients and remains fixed throughout training, and introduces no additional learnable parameters. \mathbf{R} is built by sampling a $d \times k$ matrix \mathbf{A} of i.i.d. standard Gaussian entries and computing its thin QR decomposition,

$$\mathbf{A} = \mathbf{Q} \mathbf{T}, \quad (3)$$

where $\mathbf{Q} \in \mathbb{R}^{d \times k}$ has orthonormal columns ($\mathbf{Q}^\top \mathbf{Q} = \mathbf{I}_k$) and $\mathbf{T} \in \mathbb{R}^{k \times k}$ is upper triangular. We set $\mathbf{R} := \mathbf{Q}$ and discard \mathbf{T} . Sampled once before training and fixed thereafter, this yields $\mathbf{R}^\top \mathbf{R} = \mathbf{I}_k$ exactly, is independent of any data, and adds no learnable parameters on the client. This is the standard random-projection setting under which the JL guarantee from Sect. II-B applies.

The projection reduces the communication cost from d to k scalars per sample, with compression ratio $CR = d/k \geq 1$. Only the projected representation $\tilde{\mathbf{z}}$ is transmitted to the server, and gradients are returned with respect to $\tilde{\mathbf{z}}$, so that the original activation \mathbf{z} never leaves the client.

From a privacy perspective, the projection acts as an information bottleneck. Let $I(\cdot; \cdot)$ denote the Shannon mutual information between two random variables, intuitively, the number of bits of information one carries about the other. Since $\mathbf{x} \rightarrow \mathbf{z} \rightarrow \tilde{\mathbf{z}}$ forms a Markov chain, the data-processing inequality implies $I(\mathbf{x}; \tilde{\mathbf{z}}) \leq I(\mathbf{x}; \mathbf{z})$. Thus, the projection cannot introduce new information about \mathbf{x} that were not already present in \mathbf{z} .

However, it does not eliminate information leakage, as residual instance-specific signals may still remain in $\tilde{\mathbf{z}}$. The projection reduces the overall information content, while the complementary Within-Class Compaction (see Sect. IV-D) mechanism further suppresses sample-specific variation that can be exploited by reconstruction attacks.

From a utility perspective, the projection preserves the geometric structure of the activations. As given by the JL-

lemma (see Sect. II-B), pairwise distances are approximately maintained under random projection with high probability. This is sufficient for downstream classification, where class separability primarily depends on relative distances.

C. Server-Side Liftback

A key design objective for LightSplit’s server-side components is seamless integration into existing SL architectures without requiring modifications to the underlying DNN. While the client-side design reduces information exposure and projects activations into a lower-dimensional subspace, the server-side preserves compatibility with the backbone.

Therefore, the projection $\tilde{\mathbf{z}} \in \mathbb{R}^k$ must be mapped to a d -dimensional input, compatible with the backbone g . This mapping should preserve task-relevant structure while compensating for the distribution shift induced by the projection.

We define two lift-back mechanisms (LIGHTSPLIT-F and LIGHTSPLIT-L) as trade-off between efficiency and adaptability. LIGHTSPLIT-F uses a parameter-free linear mapping, minimizing computational overhead, while LIGHTSPLIT-L employs a trainable transformation to better adapt to the projected representation and recover task-relevant structure. Both modes use the same client projection and communication budget but differ only in server-side parameterization and how the server processes incoming projected representations.

a) **LIGHTSPLIT-F- fixed linear lift-back:** LIGHTSPLIT-F is the low-parameter server mode that directly reuses the projection matrix \mathbf{R} to lift the projected representation back to the original dimensionality as:

$$\hat{\mathbf{z}} = \mathbf{R}\tilde{\mathbf{z}} = \mathbf{R}\mathbf{R}^\top \mathbf{z} \in \mathbb{R}^d. \quad (4)$$

Let $\mathbf{P} = \mathbf{R}\mathbf{R}^\top \in \mathbb{R}^{d \times d}$. Since $\mathbf{R}^\top \mathbf{R} = \mathbf{I}_k$, the matrix \mathbf{P} satisfies $\mathbf{P}^2 = \mathbf{P}$ and $\mathbf{P}^\top = \mathbf{P}$, so \mathbf{P} is the orthogonal projector onto the k -dimensional subspace $\text{range}(\mathbf{R}) \subset \mathbb{R}^d$, and $\hat{\mathbf{z}} = \mathbf{P}\mathbf{z}$ is the best Euclidean approximation to \mathbf{z} within that subspace, with residual

$$\|\mathbf{z} - \hat{\mathbf{z}}\|_2^2 = \|(\mathbf{I}_d - \mathbf{R}\mathbf{R}^\top) \mathbf{z}\|_2^2. \quad (5)$$

The residual lies entirely in the $(d-k)$ -dimensional null space of \mathbf{P} , so the lift-back is lossy by construction. The chain rule gives the gradient that the server returns to the client through the linear bottleneck: for any scalar loss \mathcal{L} that depends on \mathbf{z} only through $\tilde{\mathbf{z}} = \mathbf{R}^\top \mathbf{z}$,

$$\nabla_{\mathbf{z}} \mathcal{L} = \mathbf{R} \nabla_{\tilde{\mathbf{z}}} \mathcal{L}, \quad (6)$$

so the same fixed matrix \mathbf{R} that projects the forward activation also lifts the returned gradient back to the client’s coordinate system. The lift-back itself adds no trainable server parameters and reduces server-side computation to a single fixed matrix multiplication defined by \mathbf{R} .

b) **LIGHTSPLIT-L- learned MLP lift-back:**

LIGHTSPLIT-L replaces the fixed map of Eq. (4) with a learnable lift-back $\phi : \mathbb{R}^k \rightarrow \mathbb{R}^d$ trained jointly with g . Fig. 3 visualizes the geometry behind the two modes. The hollow circle is the original cut-layer activation $\mathbf{z} \in \mathbb{R}^d$, the blue plane is $\text{range}(\mathbf{R})$, the k -dimensional task-independent

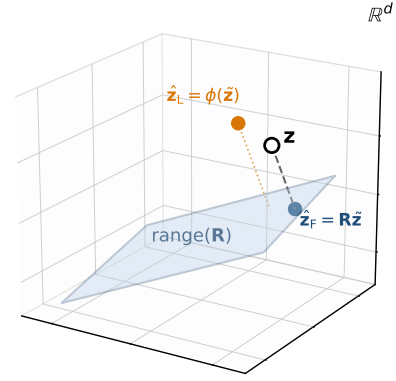


Fig. 3: Relation between the cut-layer activation, its projected representation, and the lift-back mappings. Cut-layer activation $\mathbf{z} \in \mathbb{R}^d$ (black) is projected onto the k -dimensional subspace $\text{range}(\mathbf{R})$ (shaded plane), yielding the transmitted representation $\tilde{\mathbf{z}} = \mathbf{R}^\top \mathbf{z} \in \mathbb{R}^k$. The fixed lift-back reconstructs $\hat{\mathbf{z}}_F = \mathbf{R}\tilde{\mathbf{z}}$ (blue), which lies in $\text{range}(\mathbf{R})$. The dashed line denotes the residual component between \mathbf{z} and $\hat{\mathbf{z}}_F$. The learned lift-back $\hat{\mathbf{z}}_L = \phi(\tilde{\mathbf{z}})$ (orange) maps the projected representation back into \mathbb{R}^d and is not restricted to $\text{range}(\mathbf{R})$.

subspace fixed before training. The dashed segment is the residual $\mathbf{z} - \mathbf{P}\mathbf{z}$ that the projection discards (with $\mathbf{P} = \mathbf{R}\mathbf{R}^\top$). It lies in the null space of \mathbf{P} and is invisible to the server in either mode. LIGHTSPLIT-F returns $\hat{\mathbf{z}}_F = \mathbf{R}\tilde{\mathbf{z}} = \mathbf{P}\mathbf{z}$ (blue dot): the orthogonal projection of \mathbf{z} onto the plane, pinned inside $\text{range}(\mathbf{R})$. LIGHTSPLIT-L returns $\hat{\mathbf{z}}_L = \phi(\tilde{\mathbf{z}})$ (orange dot), which sits off the plane; the dotted drop indicates that $\hat{\mathbf{z}}_L$ is no longer constrained to $\text{range}(\mathbf{R})$. Both modes operate on the same $\tilde{\mathbf{z}}$, receiving identical information about \mathbf{z} . Due to the data-processing inequality, ϕ cannot recover the discarded residual [7]. ϕ does not recover the residual, the projection discards. It only re-encodes the surviving information across \mathbb{R}^d instead of constraining it to $\text{range}(\mathbf{R})$.

Motivation. Under LIGHTSPLIT-F, the backbone g receives input pinned to the same k -dimensional plane of \mathbb{R}^d for every sample, fixed before training. To extract task features from that plane g must spend representational capacity on a global, non-spatial linear re-mapping. This matches the sed spatial inductive biases of the convolutional backbones. LIGHTSPLIT-L places that re-mapping in an MLP at the $\mathbb{R}^k \rightarrow \mathbb{R}^d$ interface absorbs the algebra cheaply and frees g ’s capacity for task-relevant features. The same adapter is also the only adaptable component in the server pipeline when g is frozen or pre-trained. Concretely, the server trains an MLP with hidden width m jointly with the backbone:

$$\hat{\mathbf{z}} = \mathbf{W}_2 \sigma(\text{BN}(\mathbf{W}_1 \tilde{\mathbf{z}})) \in \mathbb{R}^d, \quad (7)$$

with $\mathbf{W}_1 \in \mathbb{R}^{m \times k}$, $\mathbf{W}_2 \in \mathbb{R}^{d \times m}$, $\text{BN}(\cdot)$ batch normalization, and $\sigma(\cdot)$ element-wise ReLU.

The choice between LIGHTSPLIT-F and LIGHTSPLIT-L is a deployment decision for the server: the same pay-

load $\tilde{\mathbf{z}}$ is sent in both modes, so client cost, bandwidth, and adversary view are identical, and the privacy properties (Sect. IV-D) are inherited unchanged. LIGHTSPLIT-F is the minimal scheme, without learned lift-back, server-side parameters, or extra training dynamics. Thus, it is preferable when the backbone has spare capacity to absorb the rank- k restriction. LIGHTSPLIT-L is suitable when g is frozen or the inductive-bias mismatch becomes the limiting factor. As shown in Sect. V, LIGHTSPLIT-L achieves better performance LIGHTSPLIT-F on more complex benchmarks while providing similar results in remaining benchmarks.

The following subsection discusses the remaining privacy challenge of projection-based approaches: while projection reduces the overall information content, residual instance-level signals may persist in the transmitted representation. We therefore introduce Within-Class Compaction (WCC), which suppresses such variation and limits the information exploitable by reconstruction attacks.

D. Privacy Role of Within-Class Compaction

Notably, projection alone provides only limited privacy protection. While the JL property preserves class structure, it may also retain cues that can be exploited by feature-inversion and model-inversion attacks. In particular, a malicious server with access to auxiliary data can train a simulator or decoder on the observed representations. Since the projection matrix \mathbf{R} is known, the server can lift $\tilde{\mathbf{z}}$ back into the projected activation subspace, enabling it to exploit residual structure for reconstructing information about the clients’ data. Thus, while random projection reduces dimensionality, it does not eliminate all instance-specific variation in the transmitted representation that potentially allows information leakage.

To limit this leakage, we introduce Within-Class Compaction (WCC), which targets the residual instance-level variation that remains after projection. The key idea is to preserve class-discriminative structure while suppressing variability that is not required for the learning task.

This intuition can be formalized using Shannon mutual information. Treating the label y as a deterministic function of the input \mathbf{x} (as is standard in supervised learning), the chain rule of mutual information yields

$$I(\mathbf{x}; \tilde{\mathbf{z}}) = I(y; \tilde{\mathbf{z}}) + I(\mathbf{x}; \tilde{\mathbf{z}} | y). \quad (8)$$

$I(y; \tilde{\mathbf{z}})$, captures the class-discriminative signal required for prediction and should be preserved. The second term, $I(\mathbf{x}; \tilde{\mathbf{z}} | y)$, represents residual instance-specific information given the label. This term upper-bounds the information available to reconstruction attacks, and reducing it increases the inherent difficulty of recovering individual inputs.

WCC targets this residual term through a tractable surrogate. By minimizing within-class scatter in the transmitted representation, it encourages samples of the same class to form compact clusters, making $\tilde{\mathbf{z}}$ behave more like a class prototype than an instance descriptor. As a result, inputs from the same class become less distinguishable, reducing the exploitable per-sample signal while preserving class-level structure.

For a mini-batch $\{(\tilde{\mathbf{z}}_i, y_i)\}_{i=1}^b$ of size b , where $y_i \in \{1, \dots, C\}$ is the class label of sample i and C is the number of classes, let $S_c = \{i : y_i = c\}$ denote the index set of samples in class c , and define the class centroid $\boldsymbol{\mu}_c$ in the projected space as:

$$\boldsymbol{\mu}_c = \frac{1}{|S_c|} \sum_{i \in S_c} \tilde{\mathbf{z}}_i, \quad (9)$$

The WCC loss \mathcal{L}_{WCC} is then defined as:

$$\mathcal{L}_{\text{WCC}} = \sum_{c \in \mathcal{Y}_b} \frac{1}{|S_c|} \sum_{i \in S_c} \|\tilde{\mathbf{z}}_i - \boldsymbol{\mu}_c\|_2^2, \quad (10)$$

where \mathcal{Y}_b is the set of batch labels and $\|\cdot\|_2$ denotes the Euclidean norm. The loss is computed on the client, using labels that never leave the client, and adds no communication (see Appendix G).

The training objective \mathcal{L} is defined as the combination:

$$\mathcal{L} = \mathcal{L}_{\text{CE}}(\hat{y}, y) + \lambda_{\text{WCC}} \mathcal{L}_{\text{WCC}}, \quad (11)$$

where λ_{WCC} controls the compaction strength. Setting $\lambda_{\text{WCC}} = 0$ recovers projection-only training. In our evaluation we ablate $\lambda_{\text{WCC}} \in \{0, 10^{-3}, 10^{-2}, 10^{-1}, 1\}$ and observe that values in the range $[10^{-2}, 10^{-1}]$ perform consistently well.

Notably, WCC is not an adversarial loss nor trains a privacy discriminator, but a variance penalty that acts as a tractable surrogate for reducing the class-conditional per-sample signal $I(\mathbf{x}; \tilde{\mathbf{z}} | y)$. It targets the same Shannon mutual information used in Sect. IV-B, but now conditioned on the label y .

The full training procedure, including where the projection, the lift-back, and \mathcal{L}_{WCC} are placed in one mini-batch step, is formalized in Alg. 2 and Alg. 1 for the client and server respectively. App. G expands this into a step-by-step forward and backward derivation under the two-optimizer deployment that mirrors a real client-server split.

V. EVALUATION

A. Experimental Setup

a) Setup: We use the U-shaped SL protocol throughout (USL, Sec. II-A), and we vary two orthogonal axes that recur across our experiments. *(i) Client head size.* Each model in Table II is split at two cut depths reported as L1H and L2H. *(ii) Client head ownership.* The client head is either per-client (PCH) (each client i owns its own f_i) or shared SCH (a single f is shared across clients).

1) Datasets, models, and cut layers: We consider experimental setups. For the baseline utility experiments measuring model utility and compression, we aligned with the work of Rieger *et al.* [36]. For the privacy attack experiments, we adopt each attack’s public-repository configuration, mirroring their assumed victim architecture, dataset, optimizer, and hyperparameters, and insert LightSplit’s module at the specified cut.

To measure utility, we use the CIFAR-10 [27], CIFAR-100 [27], and GTSRB [39] datasets. We also use MNIST [28] and Fashion-MNIST [46] datasets in the per-sample inversion attacks, where their public artifacts support it. Following

TABLE II: Model partitions for U-shaped split learning. Head parameters shown for both Level 1 Head (L1H) and Level 2 Head (L2H) variants. The LightSplit-L MLP liftback is the *optional* server-side MLP used by LIGHTSPLIT-L mode (Linear \rightarrow BN \rightarrow ReLU \rightarrow Linear); its size depends on dataset and CR. We list the CR= 8 instantiation; values for CR= 16/32 shrink linearly with k .[‡]

Model	Dataset	L1H	L2H	Backbone	Tail	Activation	h_{MLP}	MLP*	LIGHTSPLIT-L
ResNet-18	CIFAR-10	9,536	83,520	11,166,976	5,130	$64 \times 8 \times 8$	512	2,364,928	
ResNet-18	CIFAR-100	9,536	83,520	11,166,976	51,300	$64 \times 8 \times 8$	2,048	9,447,424	
MicronNet	GTSRB	824	8,451	411,192	12,943	$29 \times 14 \times 14$	128	824,500	
SimpleCNN	FMNIST	520	4,160	435,162	5,130	$20 \times 12 \times 12$	128	417,984	

*Liftback MLP parameters at CR= 8; h_{MLP} is the per-dataset hidden dim chosen by ablation (see Appendix-F). MLP scales linearly with k , so CR= 16/32 values are $\sim 5\%$ and $\sim 8\%$ smaller respectively.

[‡]For GTSRB, MicronNet’s first max-pool is relocated from the backbone into the head so the smashed-data activation is $29 \times 14 \times 14 = 5684$ instead of the original $29 \times 28 \times 28 = 22,736$. Head/backbone parameter counts are unchanged.

Algorithm 1 LightSplit server-side training

```

1: Input: clients  $\mathcal{C}$ , rounds  $T$ , backbone  $g$ , projection dimension  $k$ , activation
   dimension  $d$ , learning rate  $\eta_g$ , mode  $m \in \{\text{LIGHTSPLIT-F}, \text{LIGHTSPLIT-L}\}$ 
2: Output: updated backbone  $g$  and lift-back  $\phi$ 
    $\triangleright$  Initialize Projection and Lift-back
3:  $\mathbf{R} \leftarrow \text{QR}(\mathcal{U}(0, 1)^{d \times k})$ 
4: if  $m = \text{LIGHTSPLIT-F}$  then
5:    $\phi \leftarrow (\bar{\mathbf{z}} \mapsto \mathbf{R}\bar{\mathbf{z}})$ 
6: else
7:    $\phi \leftarrow \text{MLP}(k, d)$ 
8: end if
9: Broadcast( $\mathbf{R}, \mathcal{C}$ )
10: for each training step  $t \in [1, T \cdot |\mathcal{C}|]$  do
11:    $C_j \leftarrow \mathcal{C}[t \bmod |\mathcal{C}|]$ 
    $\triangleright$  Receive and Lift-back Projections
12:    $\bar{\mathbf{z}} \leftarrow \text{Receive}(C_j)$ 
13:    $\bar{\mathbf{z}} \leftarrow \phi(\bar{\mathbf{z}})$ 
    $\triangleright$  Server Forward Pass
14:    $\mathbf{u} \leftarrow g(\bar{\mathbf{z}})$ 
15:   Send( $\mathbf{u}, C_j$ )
    $\triangleright$  Backpropagation and Model Update
16:    $\mathbf{g}^u \leftarrow \text{Receive}(C_j)$ 
17:    $\mathbf{g}^{\text{cut}}, \nabla_g, \nabla_\phi \leftarrow \text{Backpropagate}(\mathbf{g}^u, g, \phi)$ 
18:   Send( $\mathbf{g}^{\text{cut}}, C_j$ )
19:    $g \leftarrow g - \eta_g \nabla_g$ 
20:   if  $m = \text{LIGHTSPLIT-L}$  then
21:      $\phi \leftarrow \phi - \eta_g \nabla_\phi$ 
22:   end if
23: end for
24: return  $g$ 

```

Algorithm 2 LightSplit client-side training

```

1: Input: local dataset  $\mathcal{D}_j$ , head  $f$ , tail  $h$ , batch size  $b$ , WCC weight  $\lambda_{\text{WCC}}$ ,
   learning rate  $\eta_c$ 
2: Output: updated head  $f$  and tail  $h$ 
    $\triangleright$  Receive Projection
3:  $\mathbf{R} \leftarrow \text{Receive}(\text{server})$ 
4: for each local training step do
    $\triangleright$  Client Forward Pass and Projection
5:    $(\mathbf{x}, y) \leftarrow \text{Batch}(\mathcal{D}_j, b)$ 
6:    $\mathbf{z} \leftarrow f(\mathbf{x})$ 
7:    $\bar{\mathbf{z}} \leftarrow \mathbf{R}^T \mathbf{z}$ 
8:   Send( $\bar{\mathbf{z}}, \text{server}$ )
9:    $\mathbf{u} \leftarrow \text{Receive}(\text{server})$ 
    $\triangleright$  Client Tail and Loss Computation
10:   $\hat{y} \leftarrow h(\mathbf{u})$ 
11:   $\mathcal{L}_{\text{CE}} \leftarrow \ell_{\text{CE}}(\hat{y}, y)$ 
12:   $\mathcal{L}_{\text{WCC}} \leftarrow \text{WCC}(\bar{\mathbf{z}}, y)$ 
13:   $\mathcal{L} \leftarrow \mathcal{L}_{\text{CE}} + \lambda_{\text{WCC}} \mathcal{L}_{\text{WCC}}$ 
    $\triangleright$  Backpropagation and Model Update
14:   $\mathbf{g}^u, \nabla_h \leftarrow \text{Backpropagate}(\mathcal{L}_{\text{CE}}, h)$ 
15:  Send( $\mathbf{g}^u, \text{server}$ )
16:   $\mathbf{g}^{\text{cut}} \leftarrow \text{Receive}(\text{server})$ 
17:   $\mathbf{g}^{\bar{\mathbf{z}}} \leftarrow \mathbf{g}^{\text{cut}} + \lambda_{\text{WCC}} \nabla_{\bar{\mathbf{z}}} \mathcal{L}_{\text{WCC}}$ 
18:   $\nabla_f \leftarrow \text{Backpropagate}(\mathbf{g}^{\bar{\mathbf{z}}}, f, \mathbf{R}^T)$ 
19:   $h \leftarrow h - \eta_c \nabla_h$ 
20:   $f \leftarrow f - \eta_c \nabla_f$ 
21: end for
22: return  $f, h$ 

```

Tab. II, we used two different Head cuts for each model used (for MNIST we used the settings as Fashion-MNIST).

To ensure a comparable scenario, we used for the attack evaluation the exact training settings and hyperparameters from the released artifacts of the attacks [56], [9], [47].

Baselines: We compare LightSplit on two baselines that encompass the natural design choices at the cut layer: sending the full smashed representation. (1) **RAW** where we transmit the smashed activation unmodified and, without compression, set the upper bound on what the cut can leak. (2) **LEARNED** 1×1 (L-1) where a lightweight BottleNet-style channel bottleneck trained end-to-end with the task loss [37] is used. It is a 1×1 convolution that compresses the C -channel feature map to k channels at the client level, and a paired 1×1 convolution on the server that restores C channels. It isolates the benefit of a trainable client-side compressor, a learnable codec, without reproducing BottleNet++’s full channel-aware codec [37].

Compression ratios and their readings: Compression is defined by $CR = d/k$, comparing the original activation dimension d to the transmitted dimension k . For **LEARNED** 1×1 , compression operates along channels, so CR is approximated to the nearest realizable channel count. For **RAW**, **LEARNED** 1×1 , and LightSplit, CR jointly reflects bandwidth and information: fewer transmitted features imply less information available at the cut layer.

2) *Evaluated Attacks:* In the following, we describe the evaluated attacks and experimental setups. For each attack, we adopt the setting of the original authors’ and only insert LightSplit after the first cutting layer between Client and the Server. Across all reconstruction attacks, we evaluate LIGHTSPLIT-F: the attacker applies the lift-back to recover smashed activations and then runs the attack’s original pipeline. The attack tables and figures therefore report LIGHTSPLIT-F (LS-F). Only for the backdoor evaluation, we additionally test LIGHTSPLIT-L (LS-L).

a) *SDAR*: Simulator Decoding with Adversarial Regularization (SDAR) [56] is a passive substitute-encoder reconstruction attack: a server-side simulator/discriminator pair and a decoder are trained against the defended cut-layer payload, testing whether the transmitted representation is invertible by an adversary that can train its own client-side surrogate. Adopting the authors’ setting, we use level 7 ($L=4$) ($d=4096$, $8\times 8\times 64$) and level 4 ($L=7$) ($d=8192$, $16\times 16\times 32$) for cutting. Per-method k values, and the LPIPS₂₀ computation are listed in Appendix B. SDAR ships in two settings, USL (non-conditional decoder, labels hidden from the server) and VSL (label-conditional decoder, label-aware). While focusing on USL, we additionally run VSL as a label-aware sanity check and report it in Appendix B.

b) *UnSplit*: UnSplit [9] is a per-image gradient-matching inversion attack: an attacker-side clone of the client head is iteratively fit to the observed cut-layer activation to recover the input. We evaluate at the two MnistNet cut depths supported by the released code, $\ell\in\{2, 4\}$ ($d=1152$ and $d=1024$). The compression ratio is fixed at $CR=8$; on LIGHTSPLIT-F we sweep $\lambda_{wcc}\in\{0, 10^{-2}, 10^{-1}\}$ and add a five-seed re-run at $\lambda_{wcc}=10^{-1}$ as a sanity check on the random projection \mathbf{R} . We report *foreground-masked* MSE/SSIM/PSNR/LPIPS to avoid background-pixel inflation on MNIST/Fashion-MNIST. the masking convention and the defended-training schedule are listed in Appendix C.

c) *FORA*: The FORA [47] attack trains an inversion decoder to invert the victim’s smashed activation. We adopt the authors’ default settings with the released cut at flat dimension $d=16, 384$. We evaluate both FORA’s substitute-trained *pseudo* decoder and the paper’s reference (target-inversion) decoder, reporting SSIM/PSNR/LPIPS on the reference decoder and LPIPS only on the pseudo decoder. the rationale for the metric split, per-method k values are listed in Appendix D.

d) *Backdoor setting*: As a possible side effect, the suppression of instance-specific variation and emphasis on class-level structure might support the detection of poisoned activations. We evaluate this using the canonical BadNets trigger and label-flip setup [18] (a 3×3 corner trigger with a fixed target class) in a multi-client SL setting (CIFAR-10; defaults $n=10$, $\alpha=10^7$, $\mu=0.1$, $p=0.3$, target 0, $CR=16$; one factor varied at a time). Detection is performed using a cosine-to-consensus signature with a 3σ -MAD threshold, a commonly used approach in distributed learning settings (e.g., FoolsGold [12], FLTrust [5], CONTRA [2], SafeSplit [36]). As LightSplit’s main focus is privacy and communication efficiency, we restrict the evaluation to this standard detector and do not consider more advanced attack or defense strategies. Fig. 7 reports the per-client anomaly score under each ablation. The corresponding detection F_1 against the ground-truth malicious set is tabulated in Appendix E.

e) *Metrics*: For the utility baselines, we measure top-1 test accuracy on the task classifier. Tables III, IV, V, and VIII entries marked Δ report the change from the matched RAW baseline (Δ_{Raw}), either in percentage points or, where

explicitly stated, as a relative percentage change.

For image reconstruction attacks, we use four standard image-quality metrics:

Mean Square Error (MSE): pixel-wise mean squared error between the private image and the reconstruction. peak signal-to-noise ratio (PSNR) is computed from MSE as $-10\log_{10}(\text{MSE})$ for images scaled to $[0, 1]$; higher MSE or lower PSNR means weaker reconstruction.

Structural similarity (SSIM): compares luminance, contrast, and structure between two images, so lower SSIM means less structural similarity to the private input [43].

Learned perceptual image patch similarity (LPIPS): measures perceptual distance using deep image features, making it less tied to exact pixel alignment than MSE; higher LPIPS means the reconstruction is less perceptually similar to the target [51].

Thus, throughout the reconstruction Tables III, IV, V, VI, V, and VI, arrows point toward stronger privacy: MSE/LPIPS \uparrow and SSIM/PSNR \downarrow indicate weaker visual leakage. When images are dominated by a black background, as in the UnSplit MNIST/Fashion-MNIST runs, we additionally report foreground-masked versions of these metrics so that matched background pixels do not hide reconstruction failures.

B. Experimental Results

In the following subsections, we will detail the results of our experiments.

1) Main Comparison with Raw and Learned approaches:

Tab. III summarizes our default privacy-utility trade-off at the L2H-SCH setting. Raw activations are highly invertible across all three attacks: SDAR reaches USL level-4 SSIM 0.832, FORA’s pseudo decoder reaches LPIPS 0.467, and UNSPLIT recovers inputs nearly-pixel-perfectly at the leakiest split-2 cut, with MSE of 0.13 on MNIST and 0.30 on Fashion-MNIST.

LEARNED 1×1 mostly preserves utility, with IID accuracy dropping by only 0.5 – 3.8% on CIFAR-10, FashionMNIST, and GTSRB, with CIFAR-100 the worst case at -16.9% at a $32\times$ compression. Nevertheless, the activations transmitted remain easily invertible compared to LightSplit. SDAR SSIM falls only 16.8 – 19.9%, FORA cannot consistently maintain good LPIPS results, with values between -21.8% and $+31.7\%$ (i.e. no monotone privacy gain with higher CR), and UNSPLIT MSE jumps between -7% and $+8\%$, relative to Raw, occasionally leaking *more* than the case of NO DEFENSE.

In contrast, LightSplit, even using $\lambda_{wcc} = 0$, delivers substantially larger privacy gains against every attack and at every CR: SDAR SSIM falls 37.0%/44.2%/58.3% across $\{8\times, 16\times, 32\times\}$, FORA LPIPS rises by $+34.5\%/+36.8\%/+36.2\%$, and UNSPLIT MSE increases by up to $\times 1.27$ on MNIST and $\times 1.08 - 1.09$ on Fashion-MNIST, even at the leakiest split-2 head. Utility costs are modest on simple datasets (FashionMNIST -0.5% to -1.8% , GTSRB -2.2% to -5.8%) and grow on feature-rich ones (CIFAR-10 -3.2% to -6.0% , CIFAR-100 -5.0% to -13.7%). On CIFAR-100, LIGHTSPLIT-L recovers about half of the accuracy lost under LIGHTSPLIT-F, matching what the intuition from Sect. IV-C. For complex tasks, the

TABLE III: Effectiveness of LightSplit on maintaining privacy in terms of SSIM, LPIPS, and MSE, as well as ability to maintain utility in comparison to baseline over multiple datasets.

Method	CR	Utility Acc.: Raw / $\Delta\%$ vs. Raw					Attack metric: Raw / $\Delta\%$ vs. Raw			
		CIFAR-10 IID	CIFAR-100 IID	FMNIST IID	GTSRB IID	Non-IID mean Δ Acc	SDAR-USL SSIM \downarrow	FORA pseudo LPIPS \uparrow	UnSplit MSE _{fg} \uparrow	
RAW	1 \times	87.24	59.47	91.64	98.55	69.30	0.832	0.467	$\times 1.00 / \times 1.00$	
LIGHTSPLIT (F/L)	8 \times	-4.3% / -4.4%	-11.2% / -5.0%	-0.6% / -0.5%	-2.2% / -2.9%	-3.3% / -5.0%	-37.0%	+34.5%	+27% / +9%	
LIGHTSPLIT (F/L)	16 \times	-6.0% / -3.2%	-12.8% / -8.2%	-0.9% / -0.7%	-3.8% / -3.6%	-5.0% / -6.8%	-44.2%	+36.8%	+27% / +9%	
LIGHTSPLIT (F/L)	32 \times	-6.0% / -5.3%	-13.7% / -11.7%	-1.8% / -1.3%	-5.6% / -5.8%	-8.4% / -8.3%	-58.3%	+36.2%	+27% / +8%	
LEARNED 1 \times 1	8 \times	-0.7%	-4.1%	-0.5%	-0.5%	-2.8%	-18.5%	-18.0%	+3% / +6%	
LEARNED 1 \times 1	16 \times	-1.7%	-7.5%	-0.9%	-1.0%	-4.7%	-16.8%	+31.7%	-3% / +8%	
LEARNED 1 \times 1	32 \times	-3.8%	-16.9%	-1.0%	-1.0%	-7.5%	-19.9%	-21.8%	+8% / -7%	

Notes. Utility numbers from the L2H-CSH rows of the U-shaped sweep (Appendix Table IX). SDAR uses the USL L4 split on CIFAR-10. FORA reports the deployable pseudo decoder; the white-box reference ceiling is in Appendix D. UnSplit cells report MSE_{fg}/Raw-1 at the MnistNet split-2 cut on MNIST/Fashion-MNIST; values <0% leak more than RAW. LIGHTSPLIT attack cells reflect LIGHTSPLIT-F at $\lambda_{WCC}=0$.

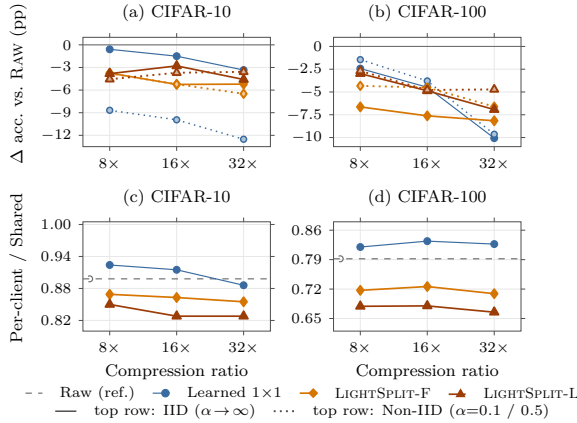


Fig. 4: Utility behaviour of LightSplit for L2H cut scenario. Top row (a, b), shows distribution stability in terms of Δ accuracy vs. matched RAW (zero line) for SCH. Bottom row (c, d), shows head-sharing cost for fixed IID-rate in terms of PCH/SCH accuracy ratio, where 1.0 means no accuracy loss from per-client heads. FashionMNIST and GTSRB show milder versions of the same trends (Appendix Table IX).

CNN backbone alone is not sufficient to deal with the rank- k restriction, and putting an MLP at the $\mathbb{R}^k \rightarrow \mathbb{R}^d$ interface stabilizes the accuracy.

2) *Utility Behavior*: Fig. 4 shows the changes in utility for CIFAR-10 and CIFAR-100 across CR, data distribution, and head-ownership configurations.

The *top row* (a, b) plots accuracy drop vs. RAW under IID and Non-IID. LightSplit’s cost stays within ≤ 8 pp on CIFAR-100 across all CRs and barely varies between IID and Non-IID scenarios. At low CRs it tracks LEARNED 1 \times 1, but at higher CRs under Non-IID LEARNED 1 \times 1 degrades faster: for CR=32 \times it loses ~ 12.5 pp on CIFAR-10 and ~ 9.6 pp on CIFAR-100, while LIGHTSPLIT-L stays within ≤ 7 pp on both. So LightSplit maintains the models’ utility *and* achieves significantly stronger privacy, as reported in Table III. Further, we observe that LIGHTSPLIT-L performs better for harder semantic tasks like CIFAR-100, while LIGHTSPLIT-F is more

robust on simpler datasets under Non-IID.

The *bottom row* (c, d) reports the PCH/SCH accuracy ratio at IID. On CIFAR-10 the PCH drop is modest, both variants of LightSplit maintain 83 – 87% of SCH accuracy and LEARNED 1 \times 1 retains $\sim 90\%$. On CIFAR-100 the drop increases: LIGHTSPLIT-L is reduced to 0.67 and LIGHTSPLIT-F to 0.71 of SCH accuracy, while LEARNED 1 \times 1 is decreased to 0.83. SCH becomes particularly relevant for complex tasks and LightSplit is more sensitive to it than LEARNED 1 \times 1. For the L2H + SCH configuration LightSplit achieves a comparable utility as RAW while delivering the privacy gains reported in Table III.

3) *Privacy Attacks*: The three attacks we test LightSplit against probe complementary surfaces: SDAR and FORA test whether a *learnable batch-level substitute* can invert the smashed activations, while UnSplit tests *per-image numerical inversion* via gradient matching.

a) *SDAR*: In Table IV we report SDAR at the default USL $L=4$, CR = 8 \times . LEARNED 1 \times 1 barely shifts the leakage profile ($\Delta_{Raw} \times 1.22$, SSIM 0.68): a trainable channel preserves the structure SDAR’s surrogate exploits. LIGHTSPLIT-F reduces SSIM almost in half from the random projection alone (0.83 \rightarrow 0.52, $\Delta_{Raw} \times 1.61$ at $\lambda_{WCC}=0$), and WCC compounds the effect on the perceptual metric: $\times 1.71$ at $\lambda_{WCC}=10^{-2}$, $\times 1.84$ at $\lambda_{WCC}=10^{-1}$, with PSNR dropping from 21.2 to 17.2 dB. Fig. 6 shows the effect of WCC on SDAR reconstructions: at $\lambda=0$ the random projection R leaves enough residual structure for the attack to recover the object shape, while at $\lambda=10^{-1}$ the reconstructions collapse further and becomes visually unidentifiable at the same CR level.

TABLE IV: SDAR reconstruction quality at the USL $L=4$, CR = 8 \times . Δ_{Raw} is the LPIPS₂₀ ratio Method/RAW; values > 1 indicate weaker visual leakage. The full $L=4/L=7$ VSL/USL CR is shown in Appendix B.

Method	MSE \uparrow	SSIM \downarrow	PSNR \downarrow	LPIPS ₂₀ \uparrow	Δ_{Raw} \uparrow
RAW	0.0076	0.8323	21.21	0.2899	$\times 1.00$
Learned 1 \times 1	0.0185	0.6784	17.33	0.3524	$\times 1.22$
LS-F, $\lambda_{WCC}=0$	0.0163	0.5244	17.88	0.4677	$\times 1.61$
LS-F, $\lambda_{WCC}=0.01$	0.0263	0.3736	15.80	0.4968	$\times 1.71$
LS-F, $\lambda_{WCC}=0.1$	0.0191	0.5269	17.18	0.5331	$\times 1.84$

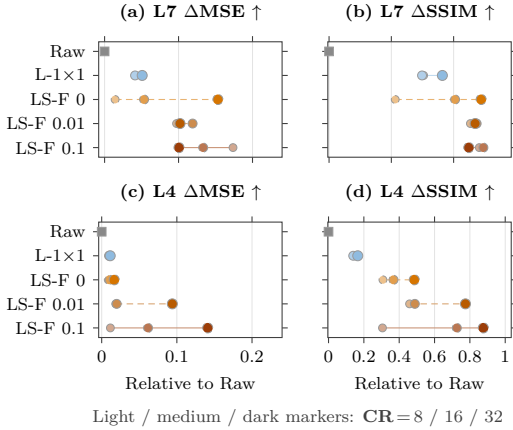


Fig. 5: USL SDAR reconstruction degradation relative to RAW at SL cutting $L=4$ and $L=7$. Positive x -values mean the defense increased MSE or reduced SSIM compared with raw SDAR. Larger values indicate weaker reconstructions.

TABLE V: FORA pseudo-attack reconstruction quality on CIFAR-10 at $CR=8$ in the U-shaped SL. $\Delta_{Raw} = LPIPS_{defense}/LPIPS_{Raw}$. Full $CR \times \lambda_{WCC}$ results are provided in Appendix D.

Method	LPIPS \uparrow	$\Delta_{Raw} \uparrow$
RAW	0.467	$\times 1.00$
LEARNED 1×1	0.383	$\times 0.82$
LIGHTSPLIT-F, $\lambda_{WCC}=0$	0.628	$\times 1.34$
LIGHTSPLIT-F, $\lambda_{WCC}=10^{-2}$	0.645	$\times 1.38$
LIGHTSPLIT-F, $\lambda_{WCC}=10^{-1}$	0.652	$\times 1.40$

Fig. 5 extends the analysis to the full USL sweep across split levels $\{4, 7\}$ and every (CR, λ_{WCC}) combination, and reveals two complementary effects of WCC on the ΔMSE and $\Delta SSIM$ relative to Raw. At $L=7$, $\lambda_{WCC}=0$ produces a wide CR-dependent spread. WCC reduces information leakage regardless of the compression ratio. At $L=4$ the outcome changes: increasing the CR alone barely adds any additional privacy benefit, but combining WCC with high CR pushes both ΔMSE and $\Delta SSIM$ far above what either term reaches in isolation. LEARNED 1×1 shows no such interaction at either level, with ΔMSE and $\Delta SSIM$ almost flat across CR. Further, we report the VSL counterpart and the full table in App. B.

b) FORA: In Table V we report FORA at the default $CR=8 \times$ slice using the *pseudo* decoder. For LEARNED 1×1 we observe $\Delta_{Raw} \times 0.82$, meaning the bottleneck leaks *more* than the RAW baseline. LIGHTSPLIT-F reverses the sign even without WCC ($\Delta_{Raw} \times 1.34$ from the random projection alone), and $\lambda_{WCC}=10^{-1}$ pushes it to $\times 1.40$ (LPIPS $0.467 \rightarrow 0.652$). Fig. 6 provides a visual confirmation on the automobile class: LIGHTSPLIT-F reconstructions degrade into noise while RAW and LEARNED 1×1 remain identifiable. The white-box reference ceiling and the full $CR \in \{8, 16, 32\} \times$ results are also reported in Appendix D. Both preserve the ordering with substantially larger ratios (up to $\Delta_{Raw} \times 7.2$).

TABLE VI: UnSplit reconstruction at the MnistNet split-2 cut. Each cell reports clean accuracy and the *worst* foreground-MSE ratio against RAW over $CR \in \{8 \times, 16 \times, 32 \times\}$. Full results are provided in Appendix C.

Method	Dataset	Acc. (%)	MSE _{fg} /Raw \uparrow
RAW	MNIST	99.0	$\times 1.00$
	F-MNIST	88.6	$\times 1.00$
Learned 1×1	MNIST	98.6–99.0	$\times 0.97$
	F-MNIST	87.9–88.6	$\times 0.93$
LIGHTSPLIT-F*	MNIST	96.7–98.0	$\times 1.27$
	F-MNIST	84.1–89.0	$\times 1.09$

* LIGHTSPLIT-F cells are bit-identical at every $\lambda_{WCC} \in \{0, 10^{-2}, 10^{-1}\}$ and every swept CR in their respective datasets.

c) UnSplit: Table VI reports UnSplit at the default split-2 cut, the shallow point where UnSplit’s gradient-matching loop is most informative. We use foreground-masked MSE so that trivially-matched zero pixels in MNIST/F-MNIST do not dominate the metric. LEARNED 1×1 stays close to the RAW baseline, with Δ_{Raw} between 0.93 and 1.08 across $CR \in \{8, 16, 32\} \times$ on both datasets and several rows dipping below 1.00. LIGHTSPLIT-F yields $\Delta_{Raw} \times 1.27$ on MNIST and $\times 1.09$ on F-MNIST, identical at all evaluated CR and $\lambda_{WCC} \in \{0, 10^{-2}, 10^{-1}\}$. Five extra random-projection seeds reproduce the same values bit-identically, and accuracy stays within 1 to 4 pp of RAW (see Appendix C).

As shown in Fig. 6, RAW recovers identifiable digit and garment silhouettes on both datasets. LEARNED 1×1 still leaks the digit shape on MNIST split-2 and remains identifiable but visibly degraded at split-4, while on F-MNIST it produces scattered white pixels with no recognizable garment class. The LIGHTSPLIT-F columns are uniformly black across datasets and splits. The split-4 results and whole-image MSE variants are reported in Appendix C and follow the same pattern.

4) Backdoor Detection Signal: While not the focus of this work, LightSplit’s ability to focus on class-level structure also highlight inconsistencies between smashed data, being typical for backdoored inputs (see Sect. V-A). To evaluate this intuition, we run a basic backdoor experiment to determine whether the compression that LightSplit introduces interferes with the cosine-similarity signal the server uses to flag malicious clients. Fig. 7 shows the full results over Dirichlet concentration α , client number n , malicious-client fraction μ , and per-client poison ratio p . Notably, the figure consistently shows across the four methods (RAW, LEARNED 1×1 , LIGHTSPLIT-F, LIGHTSPLIT-L) that malicious clients remain identifiable from the server-side backbone activations, with $|MAD-z|$ well above the 3σ threshold for every n, μ , and p . Only for highly non-IID range of panel (a) at $\alpha=0.1$ all methods, including RAW drop below 3σ . Thus, the failure is caused by the data distribution rather than the projection.

5) Ablations: We run three ablation studies: the effect of the WCC regularization strength λ_{WCC} on task accuracy (Table VII), client-count scaling (Table VIII), and the LIGHTSPLIT-L lift-back hidden width m (Fig. 8; full per-

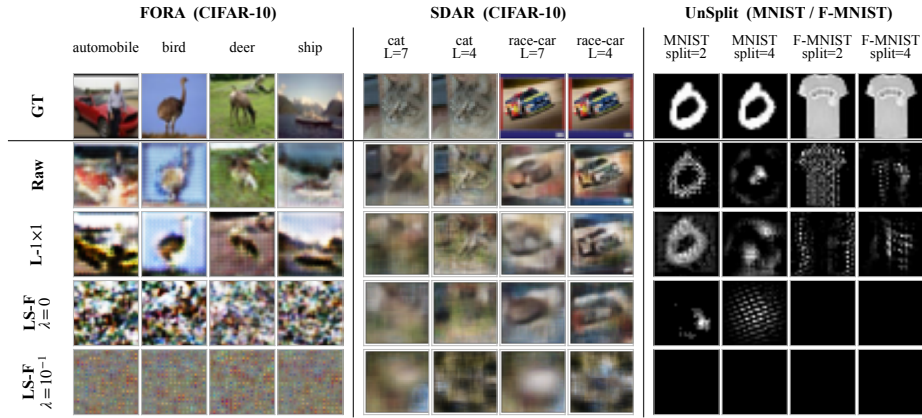


Fig. 6: Reconstruction-attack comparison across three attacks and three datasets. Each column represent individual samples. SDAR levels 4/7 and UnSplit splits 2/4.

head-config table in Appendix F).

a) *WCC strength*: The results in Tab. VII shows the impact of varying λ_{WCC} . We choose values for λ_{WCC} from 0 up to 10^{-1} on CIFAR-10 IID at $CR=8\times$, across all four head configurations (parameter counts in Table II), measuring relative accuracy loss against the matching RAW baseline.

Only L2H-SCH achieves consistent accuracy values between roughly 5 to 8% of RAW, independent of the choice for λ_{WCC} , for both LIGHTSPLIT-F and LIGHTSPLIT-L.

The other configuration L1H-SCH degrades steadily, reaching nearly a fifth below RAW at the strongest setting. Also, PCH variants reduce the accuracy. LIGHTSPLIT-F L2H-PCH starts at a 9% loss with no regularization and falls to nearly half of RAW once $\lambda_{WCC}=10^{-1}$. Notably, for L2H-PCH, accuracy significantly drops compared to the same setting for L2H-SCH, showing the benefit of the inter-client collaboration.

Our takeaway is that λ_{WCC} is a deployment-specific value, tuned jointly with head ownership and split level. For L2H-SCH LightSplit achieves consistently good results, while for other configurations a drop in utility was observed.

b) *Client-count scaling*: Table VIII varies the client count $n \in \{10, 25, 50, 100\}$ at the L2H-SCH, $CR=8\times$ default across both datasets, and reports the best test accuracy at each n along with the $n=10 \rightarrow n=100$ swing $\Delta_{10 \rightarrow 100}$.

TABLE VII: Effect of WCC regularization on accuracy across SCH, PCH and cut layer levels (CIFAR-10 IID, $\alpha \rightarrow \infty$, $n=10$, $CR=8\times$). Each cell reports the relative accuracy loss vs the matching RAW baseline.

Method	Configuration	Raw	λ_{wcc}			
			0	0.001	0.01	0.1
LIGHTSPLIT-F	L1H-SCH	86.86	-9.5%	-13.1%	-10.9%	-16.8%
LIGHTSPLIT-F	L2H-SCH	87.24	-5.0%	-6.0%	-7.5%	-5.3%
LIGHTSPLIT-F	L1H-PCH	81.28	-6.4%	-7.9%	-16.7%	-22.5%
LIGHTSPLIT-F	L2H-PCH	78.31	-9.1%	-16.4%	-33.0%	-46.9%
LIGHTSPLIT-L	L1H-SCH	86.86	-10.9%	-12.7%	-14.9%	-18.3%
LIGHTSPLIT-L	L2H-SCH	87.24	-4.6%	-5.8%	-5.7%	-5.5%
LIGHTSPLIT-L	L1H-PCH	81.28	-11.7%	-16.1%	-26.3%	-48.2%
LIGHTSPLIT-L	L2H-PCH	78.31	-10.4%	-43.2%	-70.0%	-75.2%

LIGHTSPLIT-F loses at most 0.67 pp from $n=10$ to $n=100$ on CIFAR-10 and 3.33 pp on CIFAR-100; LIGHTSPLIT-L is even flatter, losing ≤ 0.25 pp on CIFAR-10 and 2.60 pp on CIFAR-100. On CIFAR-100 the gap to RAW actually reduces with n , as the performance also for RAW drops 5.08 pp from $n=10$, while LIGHTSPLIT-L drops only 2.60 pp over the same interval. Thus, LightSplit achieves consistent results with increasing number of clients.

c) *MLP lift-back size*: Fig. 8 varies $m \in \{64, \dots, 2048\}$ at L2H-SCH, $CR=8\times$. On FashionMNIST, GTSRB, and CIFAR-10 the gap is flat from $|\phi| < 1$ M (best-to-worst spread ≤ 1.98 pp); on CIFAR-100, scaling ϕ from 1.2M to 9.4M tightens the gap by 3.11 pp ($-7.24 \rightarrow -4.13$). The lift-back's required capacity scales with task difficulty, matching the motivation in Sect. IV-C.

VI. DISCUSSION

In the previous sections, we introduced LightSplit that employs orthogonal projections building on the JL-lemma, together with the WCC constraint to limit information exposure during the training and reduce communication overhead. In the following, we discuss its security (Sect. VI-A) as and limitations (Sect. VI-B).

A. Security Considerations

We defined the adversarial threat model in Sect. III-B and derived the requirements for a secure and practical SL defense in Sect. III-C. In Sect. V, we extensively evaluated LightSplit

TABLE VIII: Client-count scaling: best test accuracy (%) at $CR=8$, L2H-SCH, IID ($\alpha \rightarrow \infty$).

Dataset	Method	$n=10$	$n=25$	$n=50$	$n=100$	$\Delta_{10 \rightarrow 100}$
CIFAR-10	RAW	87.24	85.89	88.31	88.02	+0.78
	LIGHTSPLIT-F	83.50	84.69	83.76	83.31	-0.19
	LIGHTSPLIT-L	83.42	83.80	83.82	83.40	-0.02
CIFAR-100	RAW	59.47	54.85	54.21	54.39	-5.08
	LIGHTSPLIT-F	52.83	50.56	49.52	49.50	-3.33
	LIGHTSPLIT-L	56.49	55.51	54.61	53.89	-2.60

under multiple reconstruction attacks and system settings, demonstrating that it effectively limits privacy leakage while substantially reducing communication overhead. In the following, we discuss how the design of LightSplit addresses the identified requirements and clarify its remaining limitations.

LightSplit addresses R1 (attack prevention) by limiting the amount of instance-specific information exposed at the cut layer. Clients transmit only the projected representation, irreversibly discarding information before it leaves the client. WCC further suppresses residual intra-class variation exploitable by reconstruction attacks. As shown in Sect. V, this significantly reduces reconstruction quality across multiple attacks. To preserve R2 (model utility), the projection maintains the geometric structure of the representation space, while the server-side lift-back mechanisms preserve compatibility with existing SL architectures. As demonstrated in Sect. V, LightSplit retains most of the baseline accuracy even under aggressive projection ratios. Finally, LightSplit addresses R3 (communication efficiency) by reducing the dimensionality of transmitted cut-layer activations and returned gradients from d to k , directly lowering communication overhead with only negligible client-side computation.

Out-of-Scope Threats at the Cut-Layer Interface:

LightSplit targets passive input reconstruction and does not defend against other attacks on the smashed-data channel. Label leakage attacks [29], [31] exploit cut-layer gradients or similarity-based clustering, orthogonal to per-sample activation compression. Active servers (e.g., FSHA [15]) deviate from the protocol and are caught by client-side detection mechanisms [8], [111], not by compression. Model poisoning and backdoor injection through the gradient channel are likewise outside our threat model.

Residual Leakage at the Class Level: WCC pulls same-class activations toward shared centroids, deliberately collapsing the per-sample signal that reconstruction attacks exploit. The server can still recover class-level prototypes from the

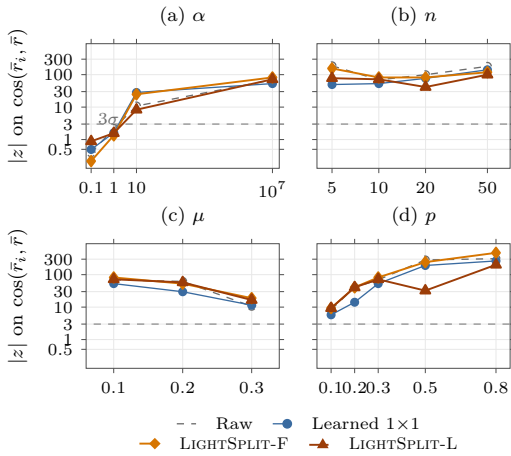


Fig. 7: Backbone-output cosine signal $\cos(\bar{r}_i, \bar{r})$. Except varied parameters, the remaining parameters are set to default values.

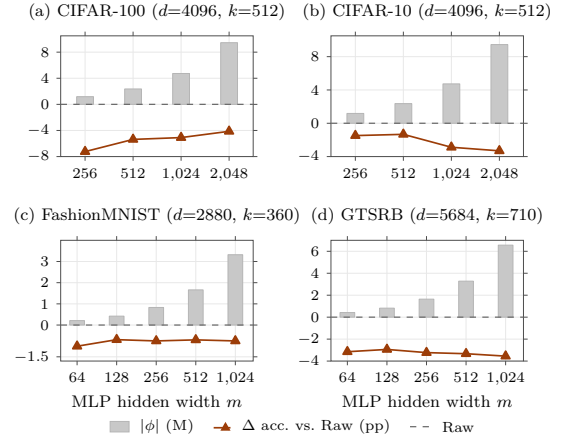


Fig. 8: Impact of MLP lift-back size on accuracy gap (L2H-SCH, CR=8). Bars: $|\phi|$ in M; line: Δ acc. vs. Raw (dashed).

smashed-data stream. We treat this as the privacy floor of LightSplit: an attacker can at best learn what an average sample of a given class looks like, not the specific input.

B. Limitations

We discuss LightSplit’s limitations and how they affect efficiency and practical applicability.

Restriction to Attacks Analyzing Smashed Data: LightSplit limits sample-specific information in smashed activations and addresses privacy risks from a curious server. White-box inference attacks that exploit shared model updates are a separate threat. LightSplit operates solely on smashed data and provides no protection against them. Sharing model updates is a design choice that can be adapted to the threat model, whereas transmitting smashed activations is fundamental to SL. We therefore focus on the cut-layer interface and leave shared-parameter settings to future work.

Formal Guarantees: LightSplit does not provide formal privacy guarantees. Instead, effectiveness is established by extensive empirical evaluation. Where formal guarantees are required, LightSplit can be combined with techniques such as differential privacy [1].

Overhead through Learnable Backlifting: LIGHTSPLIT-L uses a trainable MLP for lift-back, adding parameters and compute. This cost falls on the server, assumed to have sufficient resources (see Sect. III-A). In resource-constrained scenarios, LIGHTSPLIT-F provides a parameter-free alternative. As shown in Sect. V, the performance gap is tolerable.

VII. RELATED WORK

A. Privacy Threats at the Split Interface

In SL, raw data stays on the client, but the smashed-data interface still leaks substantial private information. In our work, we focus on *training-time* attacks: the server exploits the smashed-data stream observed during collaborative training. *Inference* attacks [22], [49] target a frozen model at deployment and are outside the scope of our work.

a) *Passive reconstruction attacks*: Gradient-based methods (DLG [55], iDLG [52], Inverting Gradients [16]) recover training data from gradient signals. In SL the threat is amplified: the server observes *per-sample* activations rather than aggregated updates. More recent attacks train a surrogate of the client encoder. UnSplit [9] alternates between optimising a clone encoder and a candidate input from the smashed-data stream, requiring only the client’s architecture and no auxiliary data. PCAT [14] drops the architecture assumption and builds a pseudo-client from the server’s own evolving checkpoints. FORA [47] trains a substitute encoder by feature-level transfer on public data. SDAR [56] is the current state of the art among passive attacks. It trains a simulator \tilde{f} on auxiliary data while keeping the server’s backbone g frozen. The attack exploits unintentional memorisation: g , co-trained with the real client encoder f , retains distributional information about the private data [6]. Two adversarial discriminators align the simulator’s activations with the client’s and force the decoded outputs to look realistic. SDAR matches the reconstruction quality of the active attack FSHA [15] while remaining fully passive. These surrogate attacks interpret the smashed-data distribution rather than inverting it analytically. A compression scheme that preserves task structure may therefore preserve enough signal to train them. We evaluate this directly.

b) *Active reconstruction attacks and detection*: FSHA [15] reconstructs inputs by hijacking the client’s encoder through manipulated gradients. Such protocol deviations are detectable [8], [11], leaving passive reconstruction as the primary practical threat and our main focus.

c) *Label leakage*: Cut-layer gradients can reveal training labels [29], and similarity-based clustering achieves label inference at the same interface [31]. Label leakage is outside our focus and left to future work.

B. Existing Defenses

a) *Representation perturbation*: NoPeek [42] penalizes input-activation correlation via distance correlation. Shredder [34] injects learned additive noise. DISCO [38] learns a pruning filter that obfuscates sensitive channels at inference time. Patch shuffling [48] permutes spatial patches in vision transformers. None of these reduces the communication payload, and adaptive attackers can defeat them by learning latent privacy features from the defended representations [56]. Because LightSplit targets joint compression and privacy, we compare against compression baselines at matched ratios.

b) *Cryptographic mechanisms*: FedVS [30] employs secret sharing to provide information-theoretic confidentiality of uploaded embeddings. Homomorphic encryption (HE) has also been proposed for privacy-preserving neural network computation [17], enabling the server to process ciphertexts without observing plaintext activations, at orders-of-magnitude computational overhead unsuitable for edge deployments.

C. Communication Compression at the Cut Layer

Top- k sparsification transmits the k largest activations and their indices [53]; mask-encoded variants replace the indices

with a bit-mask [54]. Both expose which positions are most active per input. Learned codecs train an encoder/decoder pair across the cut layer (BottleNet++ [37], FrankenSplit [13], the latter additionally requiring ImageNet pretraining), adding trainable parameters and forward-pass cost to the client. SplitFC [35] drops low-variance features and quantizes the rest with closed-form adaptive levels: parameter-free on the client but still reveals which positions are kept. C3-SL [23] superposes a batch of features via circular convolution with fixed random keys, reducing transmissions per round but not the per-sample payload.

D. Random Projections in Distributed Learning

Random projections appear in distributed learning, but applied to different objects: RanPAC [32] projects pretrained features for continual learning, Han et al. [20] project local model parameters for personalized FL, and ProjPert [10] projects backward gradients for label protection in vertical FL. To our knowledge, no prior work applies a random projection at the SL cut layer for per-sample activation compression.

E. Positioning Our Approach

Existing methods leave a gap that motivates our work. Privacy mechanisms do not compress. Compression mechanisms either leak structural information (top- k and variants), add client-side overhead (learned codecs), or do not reduce the per-sample payload (C3-SL). No existing method simultaneously compresses, avoids client overhead, and restructures the server’s observation under a semi-honest threat model.

We address this gap with a fixed, non-trainable orthogonal projection at the cut layer. Clients map their d -dimensional activation to k dimensions via \mathbf{R} , reducing the per-sample payload by d/k without trainable client parameters. The server, which knows \mathbf{R} , either lifts back via \mathbf{R}^\top (LIGHTSPLIT-F) or applies a small learned module on the compressed representation (LIGHTSPLIT-L). Both variants differ only in server-side capacity. An optional WCC regularizer pulls same-class activations toward shared centroids, removing the per-sample signal that reconstruction attacks exploit while preserving class separability. The result is a representation limiting attackers to recovering class-level prototypes, not a private input.

We do not claim formal privacy guarantees. Formal results for JL projections require added noise [3], [25]. We add none and instead measure the privacy benefit empirically under state-of-the-art attacks with full knowledge of \mathbf{R} .

REFERENCES

- [1] Martin Abadi, Andy Chu, Ian Goodfellow, H Brendan McMahan, Ilya Mironov, Kunal Talwar, and Li Zhang. Deep learning with differential privacy. In *CCS*, 2016.
- [2] Sana Awan, Bo Luo, and Fengjun Li. CONTRA: Defending against poisoning attacks in federated learning. In *ESORICS*, volume 12972. Springer, 2021.
- [3] Jeremiah Blocki, Avrim Blum, Anupam Datta, and Or Sheffet. The Johnson–Lindenstrauss transform itself preserves differential privacy. In *FOCS*, 2012.
- [4] Ashish Bora, Ajil Jalal, Eric Price, and Alexandros G. Dimakis. Compressed sensing using generative models. In *ICML*, 2017.

- [5] Xiaoyu Cao, Minghong Fang, Jia Liu, and Neil Zhenqiang Gong. FLTrust: Byzantine-robust federated learning via trust bootstrapping. In *NDSS*, 2021.
- [6] Nicholas Carlini, Chang Liu, Úlfar Erlingsson, Jernej Kos, and Dawn Song. The Secret Sharer: Evaluating and testing unintended memorization in neural networks. In *USENIX Security*, 2019.
- [7] Thomas M. Cover and Joy A. Thomas. *Elements of Information Theory*. Wiley-Interscience, 2 edition, 2006.
- [8] Ege Erdogan, Alptekin Kupcu, and A. Ercument Cicek. SplitGuard: Detecting and mitigating training-hijacking attacks in split learning. In *WPES*, 2022.
- [9] Ege Erdogan, Alptekin Kupcu, and A. Ercument Cicek. UnSplit: Data-oblivious model inversion, model stealing, and label inference attacks against split learning. In *Workshop on Privacy in the Electronic Society*, 2022.
- [10] Fangcheng Fu, Xuanyu Wang, Jiawei Jiang, Huanran Xue, and Bui Cui. ProjPert: Projection-Based Perturbation for Label Protection in Split Learning Based Vertical Federated Learning. *IEEE Transactions on Knowledge & Data Engineering*, 36(07):3417–3428, July 2024.
- [11] Jiayun Fu, Xiaojing Ma, Bin B Zhu, Pingyi Hu, Ruixin Zhao, Yaru Jia, Peng Xu, Hai Jin, and Dongmei Zhang. Focusing on pinocchio’s nose: A gradients scrutinizer to thwart split-learning hijacking attacks using intrinsic attributes. In *NDSS*, 2023.
- [12] Clement Fung, Chris J. M. Yoon, and Ivan Beschastnikh. The limitations of federated learning in sybil settings. In *International Symposium on Research in Attacks, Intrusions and Defenses (RAID)*, 2020.
- [13] Alireza Furutanpey, Philipp Raith, and Schahram Dustdar. Frankensplit: Efficient neural feature compression with shallow variational bottleneck injection for mobile edge computing. *IEEE Transactions on Mobile Computing*, 23(12):10770–10786, 2024.
- [14] Xinben Gao and Lan Zhang. PCAT: Functionality and data stealing from split learning by Pseudo-Client attack. In *USENIX Security*. USENIX Association, 2023.
- [15] Grzegorz Gawron and Philip Stubbings. Feature space hijacking attacks against differentially private split learning. *arXiv preprint arXiv:2201.04018*, 2022.
- [16] Jonas Geiping, Hartmut Bauermeister, Hannah Dröge, and Michael Moeller. Inverting gradients-how easy is it to break privacy in federated learning? *NeurIPS*, 2020.
- [17] Ran Gilad-Bachrach, Nathan Dowlin, Kim Laine, Kristin Lauter, Michael Naehrig, and John Wernsing. CryptoNets: Applying neural networks to encrypted data with high throughput and accuracy. In *ICML*, 2016.
- [18] Tianyu Gu, Brendan Dolan-Gavitt, and Siddharth Garg. BadNets: Identifying vulnerabilities in the machine learning model supply chain. *arXiv preprint arXiv:1708.06733*, 2017.
- [19] Otkrist Gupta and Ramesh Raskar. Distributed learning of deep neural network over multiple agents. *Journal of Network and Computer Applications*, 116:1–8, 2018.
- [20] Yuze Han, Xiang Li, Shiyun Lin, and Zhihua Zhang. A random projection approach to personalized federated learning: Enhancing communication efficiency, robustness, and fairness. *Journal of Machine Learning Research*, 25(380):1–88, 2024.
- [21] Kaiming He, Xiangyu Zhang, Shaoqing Ren, and Jian Sun. Deep residual learning for image recognition. In *CVPR*, 2016.
- [22] Zecheng He, Tianwei Zhang, and Ruby B. Lee. Model inversion attacks against collaborative inference. In *ACSAC*, 2019.
- [23] Cheng-Yen Hsieh, Yu-Chuan Chuang, and An-Yeu Wu. C3-SL: Circular convolution-based batch-wise compression for communication-efficient split learning. In *IEEE International Workshop on Machine Learning for Signal Processing (MLSP)*, 2022.
- [24] William Johnson and Joram Lindenstrauss. Extensions of lipschitz maps into a hilbert space. *Contemporary Mathematics*, 26:189–206, 01 1984.
- [25] Krishnamurthy Korthupadi, Aleksandra Korolova, Ilya Mironov, and Nina Mishra. Privacy via the Johnson–Lindenstrauss transform. *Journal of Privacy and Confidentiality*, 5(1), 2013.
- [26] Diederik P. Kingma and Jimmy Ba. Adam: A method for stochastic optimization. In *ICLR*, 2015.
- [27] Alex Krizhevsky. Learning multiple layers of features from tiny images. Technical report, University of Toronto, 2009.
- [28] Y. Lecun, L. Bottou, Y. Bengio, and P. Haffner. Gradient-based learning applied to document recognition. *Proceedings of the IEEE*, 86(11):2278–2324, 1998.
- [29] Oscar Li, Jiankai Sun, Xin Yang, Weihao Gao, Hongyi Zhang, Junyuan Xie, Virginia Smith, and Chong Wang. Label leakage and protection in two-party split learning. In *ICLR*, 2022.
- [30] Songze Li, Duanyi Yao, and Jin Liu. FedVS: Straggler-resilient and privacy-preserving vertical federated learning for split models. In *ICML*, 2023.
- [31] Junlin Liu, Xinchun Lyu, Qimei Cui, and Xiaofeng Tao. Similarity-based label inference attack against training and inference of split learning. *IEEE Transactions on Information Forensics and Security*, 19:2881–2895, 2024.
- [32] Mark D McDonnell, Dong Gong, Amin Parvaneh, Ehsan Abbasnejad, and Anton Van den Hengel. Ranpac: Random projections and pre-trained models for continual learning. In *NeurIPS*, 2023.
- [33] Brendan McMahan, Eider Moore, Daniel Ramage, Seth Hampson, and Blaise Aguera y Arcas. Communication-efficient learning of deep networks from decentralized data. In *International Conference on Artificial Intelligence and Statistics (AISTATS)*. Pmlr, 2017.
- [34] Fatemehsadat Mirehghallah, Mohammadkazem Taram, Prakash Ramrakhiani, Ali Jalali, Dean Tullsen, and Hadi Esmaeilzadeh. Shredder: Learning noise distributions to protect inference privacy. In *International Conference on Architectural Support for Programming Languages and Operating Systems (ASPLOS)*, 2020.
- [35] Yongjeong Oh, Jaeho Lee, Christopher Brinton, and Yo-Seb Jeon. Communication-efficient split learning via adaptive feature-wise compression. *IEEE Transactions on Neural Networks and Learning Systems*, PP:1–15, 01 2025.
- [36] Phillip Rieger, Alessandro Pegoraro, Kavita Kumari, Tigist Abera, Jonathan Knauer, and Ahmad-Reza Sadeghi. SafeSplit: A novel defense against client-side backdoor attacks in split learning. In *NDSS*, 2025.
- [37] Jiawei Shao and Jun Zhang. Bottleneck++: An end-to-end approach for feature compression in device-edge co-inference systems. In *IEEE International Conference on Communications Workshops (ICC Workshops)*, 2020.
- [38] Abhishek Singh, Ayush Chopra, Ethan Garza, Emily Zhang, Praneeth Vepakomma, Vivek Sharma, and Ramesh Raskar. DISCO: Dynamic and invariant sensitive channel obfuscation for deep neural networks. In *CVPR*, 2021.
- [39] Johannes Stalkamp, Marc Schlipf, Jan Salmen, and Christian Igel. The german traffic sign recognition benchmark: a multi-class classification competition. In *international joint conference on neural networks*. IEEE, 2011.
- [40] Chandra Thapa, Pathum Chamikara Mahawaga Arachchige, Seyit Camtepe, and Lichao Sun. SplitFed: When federated learning meets split learning. In *AAAI*, 2022.
- [41] Praneeth Vepakomma, Otkrist Gupta, Tristan Swedish, and Ramesh Raskar. Split learning for health: Distributed deep learning without sharing raw patient data. *arXiv preprint arXiv:1812.00564*, 2018.
- [42] Praneeth Vepakomma, Abhishek Singh, Otkrist Gupta, and Ramesh Raskar. Nopeek: Information leakage reduction to share activations in distributed deep learning. In *International Conference on Data Mining Workshops (ICDMW)*. IEEE, 2020.
- [43] Zhou Wang, A.C. Bovik, H.R. Sheikh, and E.P. Simoncelli. Image quality assessment: from error visibility to structural similarity. *IEEE Transactions on Image Processing*, 13(4):600–612, 2004.
- [44] Di Wu, Rehmat Ullah, Philip Rodgers, Peter Kilpatrick, Ivor Spence, and Blesson Varghese. EcoFed: Efficient Communication for DNN Partitioning-Based Federated Learning. *IEEE Transactions on Parallel & Distributed Systems*, 35(03):377–390, March 2024.
- [45] Wen Wu, Mushu Li, Kaige Qu, Conghao Zhou, Xuemin Shen, Weihua Zhuang, Xu Li, and Weisen Shi. Split learning over wireless networks: Parallel design and resource management. *IEEE Journal on Selected Areas in Communications*, 41(4):1051–1066, 2023.
- [46] Han Xiao, Kashif Rasul, and Roland Vollgraf. Fashion-MNIST: A novel image dataset for benchmarking machine learning algorithms. *arXiv preprint arXiv:1708.07747*, 2017.
- [47] Xiaoyang Xu, Mengda Yang, Wenzhe Yi, Ziang Li, Juan Wang, Hongxin Hu, Yong Zhuang, and Yaxin Liu. A stealthy wrongdoer: Feature-oriented reconstruction attack against split learning. In *CVPR*, 2024.
- [48] Dixi Yao, Liyao Xiang, Hengyuan Xu, Hangyu Ye, and Yingqi Chen. Privacy-preserving split learning via patch shuffling over transformers. In *IEEE International Conference on Data Mining (ICDM)*, 2022.
- [49] Yupeng Yin, Xianglong Zhang, Huanle Zhang, Feng Li, Yue Yu, Xiuzhen Cheng, and Pengfei Hu. Ginver: Generative model inversion attacks against collaborative inference. In *WWW*, 2023.

- [50] Fangchao Yu, Lina Wang, Bo Zeng, Kai Zhao, Zhi Pang, and Tian Wu. How to backdoor split learning. *Neural Networks*, 168:326–336, 2023.
- [51] Richard Zhang, Phillip Isola, Alexei A. Efros, Eli Shechtman, and Oliver Wang. The unreasonable effectiveness of deep features as a perceptual metric. In *CVPR*, 2018.
- [52] Bo Zhao, Konda Reddy Mopuri, and Hakan Bilen. idlg: Improved deep leakage from gradients. *arXiv preprint arXiv:2001.02610*, 2020.
- [53] Fei Zheng, Chaochao Chen, Lingjuan Lyu, and Binhui Yao. Reducing communication for split learning by randomized top-k sparsification. In *International Joint Conference on Artificial Intelligence*, 2023.
- [54] Wenxuan Zhou, Zhihao Qu, Shen-Huan Lyu, Miao Cai, and Baoliu Ye. Mask-encoded sparsification: Mitigating biased gradients in communication-efficient split learning. In *ECAI - European Conference on Artificial Intelligence*, Frontiers in Artificial Intelligence and Applications. IOS Press, 2024.
- [55] Ligeng Zhu, Zhijian Liu, and Song Han. Deep leakage from gradients. In *NeurIPS*, 2019.
- [56] Xiaochen Zhu, Xinjian Luo, Yuncheng Wu, Yangfan Jiang, Xiaokui Xiao, and Beng Chin Ooi. Passive inference attacks on split learning via adversarial regularization. In *NDSS*, 2025.

APPENDIX

Our appendix completes the per-attack and per-configuration sweeps that the main eval cross-references, and gives the step-by-step training derivation that Sec. IV-D defers. Sec. A reports the full utility grid across every (dataset, distribution, head ownership, head depth, CR) cell; Sec. B, Sec. C, and Sec. D give the complete per-method, per-CR, per- λ_{WCC} tables for the three reconstruction attacks evaluated, with the SDAR reconstruction grids in Sec. B; Sec. E reports the cosine-to-consensus signal on the server-input smashed payload alongside the F_1 detection grid that backs the main-text backdoor claim; Sec. F ablates the LIGHTSPLIT-L lift-back hidden width that Sec. A reads off; and Sec. G walks through one mini-batch of LightSplit training under the two-optimizer client/server deployment to verify that adding \mathcal{L}_{WCC} leaves the cut-interface protocol of plain U-shaped split learning unchanged. Notation and method names follow the main paper throughout.

A. Full utility baseline experiments

Table IX reports the complete utility grid behind the main-text utility analysis: best test accuracy for every (dataset, distribution, head ownership, head depth, CR) cell, with Δ measured against the matched RAW baseline at the same head depth, head ownership, and dataset. The four head configurations are the cross of L1H/L2H with SCH/PCH, so each row group corresponds to one system configuration. LIGHTSPLIT-L uses the per-dataset hidden width selected by the ablation in Sec. F: cifar10=512, cifar100=2048, fmnist=128, gtsrb=128. The [†] rows on Fashion-MNIST and GTSRB mark cells where LEARNED 1×1 cannot realise the requested CR exactly: channel-count quantisation forces an effective compression of 10×/20× on Fashion-MNIST and $\sim 10\times/29\times$ on GTSRB instead of 8×/16×. We list each daggered run under its requested- CR column for cross-row comparability, with the accuracy measured at the realised (channel-quantised) CR.

B. SDAR: full attack configuration

We adopt the SDAR [56] pipeline at the upstream defaults; the only edit is the insertion of the method object at the cut,

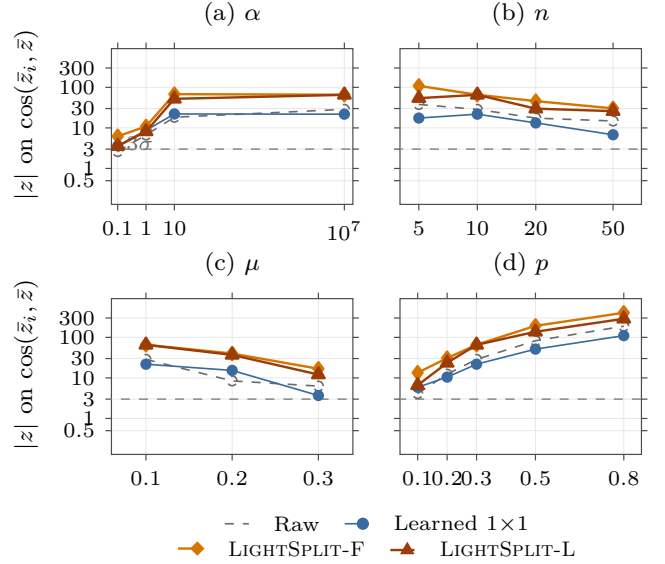


Fig. 9: **Server-input cosine signal** $\cos(\bar{z}_i, \bar{z})$. Malicious-client $|\text{MAD-z-score}|$ vs. each ablation axis; in every panel the swept parameter is varied while the rest are held at the defaults reported in Fig. 7.

applied identically to the target path and to the simulator path so that RAW reduces to the released attack.

Per-method k values. For LIGHTSPLIT-F at L7, $\text{CR}=d/k \in \{8, 16, 32\}$ fixes $k \in \{512, 256, 128\}$; at L4 the same ratios fix $k \in \{1024, 512, 256\}$. The flat activation is projected onto an orthonormal fixed random basis, then lifted back into the original smashed-feature shape before g . LEARNED 1×1 keeps the same nominal CR with $k_{\text{ch}} \in \{8, 4, 2\}$ at L7 and $\{4, 2, 1\}$ at L4.

LPIPS₂₀ computation. MSE and SSIM are the full client-set averages printed by SDAR’s `evaluate()`; PSNR is computed from that MSE as $-10\log_{10}(\text{MSE})$ with image range $[0, 1]$. LPIPS₂₀ is computed afterward with LPIPS-Alex on the saved 20-image reconstruction grid, because the SDAR artifacts save loss histories and PNGs but not full-dataset reconstruction tensors.

Figures 10–21 provide the qualitative counterpart to Sec. B. Each figure fixes one combination of split level $\{4, 7\}$, training mode $\{\text{USL}, \text{VSL}\}$, and compression ratio $\text{CR} \in \{8, 16, 32\}$, and shows reconstructions from RAW, LEARNED 1×1, and LIGHTSPLIT-F at $\lambda_{WCC} \in \{0, 10^{-2}, 10^{-1}\}$ on the same 16 client images. Reading down a column of any figure shows the effect of WCC at fixed CR; reading across figures at fixed method shows the effect of CR at fixed level and training mode.

C. UnSplit:full attack configuration

We adopt the UnSplit [9] pipeline at the upstream defaults; the only edit is the insertion of the method object between the client head and the server backbone. The victim is the MnistNet architecture from the released attack repository,

TABLE IX: U-shaped split learning: best test accuracy (%) without reconstruction loss ($\lambda_r=0$), merging SCH and PCH (per-client) head settings across L1H (shallow) and L2H cuts. Δ vs. matching RAW baseline (same dataset, distribution, depth, head). LIGHTSPLIT-L uses per-dataset `mlp_hidden` (cifar10=512, cifar100=2048, fmnist=128, gtsrb=128) selected via the ablation in Sec. F. GTSRB uses the revised head cut (activation_dim=5684). [†] LEARNED 1×1 channel-quantization on FashionMNIST (in_ch=20) and GTSRB (in_ch=29) yields effective compression $10\times/20\times$ (FMNIST) and $\sim 10\times/29\times$ (GTSRB) instead of $8\times/16\times/32\times$; cells are placed under the CR column.

Method	k	CR	Depth	Head	CIFAR-10				CIFAR-100				FashionMNIST				GTSRB			
					$\alpha=0.1$		$\alpha\rightarrow\infty$		$\alpha=0.5$		$\alpha\rightarrow\infty$		$\alpha=0.1$		$\alpha\rightarrow\infty$		$\alpha=0.1$		$\alpha\rightarrow\infty$	
					Acc	Δ	Acc	Δ	Acc	Δ	Acc	Δ	Acc	Δ	Acc	Δ	Acc	Δ	Acc	Δ
Raw	4096	1 \times	L1H	SCH	46.69	-	86.86	-	58.11	-	59.56	-	86.11	-	91.86	-	96.44	-	97.61	-
			L1H	PCH	22.82	-	81.28	-	39.78	-	49.95	-	57.21	-	88.82	-	80.80	-	96.10	-
			L2H	SCH	49.08	-	87.24	-	57.46	-	59.47	-	72.21	-	91.64	-	98.44	-	98.55	-
			L2H	PCH	22.67	-	78.31	-	31.65	-	47.09	-	56.03	-	88.67	-	79.58	-	97.66	-
LIGHTSPLIT-F	512	8 \times	L1H	SCH	41.56	-5.13	76.34	-10.52	44.87	-13.24	43.71	-15.85	82.41	-3.70	90.27	-1.59	87.39	-9.06	90.19	-7.42
			L1H	PCH	21.31	-1.51	71.79	-9.49	23.45	-16.33	38.62	-11.33	52.31	-4.90	86.72	-2.10	56.69	-24.11	88.17	-7.93
			L2H	SCH	45.29	-3.79	83.50	-3.74	53.13	-4.33	52.83	-6.64	74.00	+1.79	91.08	-0.56	95.75	-2.69	96.42	-2.13
			L2H	PCH	20.01	-2.66	72.57	-5.74	24.04	-7.61	37.89	-9.20	51.49	-4.54	87.17	-1.50	64.62	-14.96	94.06	-3.59
	256	16 \times	L1H	SCH	36.52	-10.17	72.70	-14.16	42.16	-15.95	42.20	-17.36	79.72	-6.39	89.75	-2.11	84.96	-11.49	87.47	-10.14
			L1H	PCH	17.25	-5.57	67.57	-13.71	22.27	-17.51	35.69	-14.26	51.72	-5.49	86.13	-2.69	42.89	-37.91	85.76	-10.35
			L2H	SCH	43.86	-5.22	81.99	-5.25	52.95	-4.51	51.85	-7.62	72.59	+0.38	90.83	-0.81	94.05	-4.39	94.77	-3.78
			L2H	PCH	19.78	-2.89	70.76	-7.55	23.18	-8.47	37.62	-9.47	51.79	-4.24	86.38	-2.29	54.10	-25.48	91.69	-5.97
	128	32 \times	L1H	SCH	34.02	-12.67	69.97	-16.89	38.59	-19.52	39.04	-20.52	76.75	-9.36	89.26	-2.60	77.59	-18.85	83.19	-14.42
			L1H	PCH	17.82	-5.00	63.92	-17.36	18.11	-21.67	32.97	-16.98	51.21	-6.00	85.68	-3.14	39.77	-41.03	77.42	-18.69
			L2H	SCH	42.59	-6.49	82.03	-5.21	50.85	-6.61	51.31	-8.16	70.78	-1.43	90.00	-1.64	89.81	-8.63	93.07	-5.48
			L2H	PCH	19.88	-2.79	70.13	-8.18	18.25	-13.40	36.37	-10.72	49.96	-6.07	86.20	-2.47	46.65	-32.93	88.60	-9.06
LIGHTSPLIT-L	512	8 \times	L1H	SCH	43.56	-3.13	76.72	-10.14	48.05	-10.06	45.89	-13.67	69.18	-16.93	89.97	-1.89	82.21	-14.24	89.47	-8.14
			L1H	PCH	24.26	+1.44	72.58	-8.70	26.68	-13.10	41.90	-8.05	45.73	-11.48	84.69	-4.13	46.83	-33.97	87.08	-9.03
			L2H	SCH	44.52	-4.56	83.42	-3.82	54.77	-2.69	56.49	-2.98	70.87	-1.34	91.18	-0.46	93.20	-5.24	95.71	-2.84
			L2H	PCH	22.00	-0.67	70.93	-7.38	26.96	-4.69	38.33	-8.76	47.59	-8.44	85.38	-3.29	61.76	-17.82	94.87	-2.79
	256	16 \times	L1H	SCH	47.50	+0.81	75.00	-11.86	45.68	-12.43	43.18	-16.38	65.43	-20.68	89.29	-2.57	79.14	-17.30	87.14	-10.47
			L1H	PCH	23.13	+0.31	70.52	-10.76	26.00	-13.78	38.59	-11.36	37.29	-19.92	83.41	-5.41	35.19	-45.61	86.54	-9.56
			L2H	SCH	45.38	-3.70	84.45	-2.79	52.68	-4.78	54.60	-4.87	70.64	-1.57	91.04	-0.60	89.52	-8.92	94.98	-3.57
			L2H	PCH	17.85	-4.82	69.95	-8.36	26.21	-5.44	37.12	-9.97	29.29	-26.74	84.71	-3.96	57.09	-22.49	91.70	-5.95
	128	32 \times	L1H	SCH	42.79	-3.90	71.84	-15.02	42.50	-15.61	39.50	-20.06	61.17	-24.94	88.77	-3.09	73.18	-23.26	83.58	-14.03
			L1H	PCH	20.31	-2.51	66.35	-14.93	23.29	-16.49	34.92	-15.03	23.97	-33.24	81.12	-7.70	30.80	-50.00	78.04	-18.07
			L2H	SCH	45.50	-3.58	82.65	-4.59	52.74	-4.72	52.54	-6.93	69.00	-3.21	90.45	-1.19	87.05	-11.39	92.80	-5.75
			L2H	PCH	17.62	-5.05	68.45	-9.86	24.79	-6.86	34.94	-12.15	36.03	-20.00	83.83	-4.84	49.64	-29.94	90.21	-7.44
Learned 1×1	512	8 \times	L1H	SCH	47.72	+1.03	85.54	-1.32	56.67	-1.44	56.81	-2.75	82.25 [†]	-3.86	90.65 [†]	-1.21	96.61 [†]	+0.17	97.39 [†]	-0.22
			L1H	PCH	15.87	-6.95	83.04	+1.76	43.10	+3.32	49.97	+0.02	67.80 [†]	+10.59	88.85 [†]	+0.03	82.79 [†]	+2.00	95.09 [†]	-1.01
			L2H	SCH	40.40	-8.68	86.65	-0.59	56.01	-1.45	57.04	-2.43	75.47 [†]	+3.26	91.20 [†]	-0.44	97.60 [†]	-0.84	98.01 [†]	-0.54
			L2H	PCH	16.52	-6.15	80.09	+1.78	33.84	+2.19	46.78	-0.31	60.42 [†]	+4.39	89.05 [†]	+0.38	84.45 [†]	+4.87	97.35 [†]	-0.31
	256	16 \times	L1H	SCH	39.13	-7.56	83.32	-3.54	50.68	-7.43	50.45	-9.11	79.42 [†]	-6.69	89.25 [†]	-2.61	95.00 [†]	-1.45	95.87 [†]	-1.74
			L1H	PCH	14.87	-7.95	80.17	-1.11	42.16	+2.38	47.88	-2.07	68.34 [†]	+11.13	88.44 [†]	-0.38	82.79 [†]	+1.99	94.51 [†]	-1.59
			L2H	SCH	39.14	-9.94	85.74	-1.50	53.67	-3.79	54.99	-4.48	74.93 [†]	+2.72	90.82 [†]	-0.82	96.30 [†]	-2.14	97.55 [†]	-1.01
			L2H	PCH	23.69	+1.02	78.45	+0.14	31.50	-0.15	45.86	-1.23	59.97 [†]	+3.94	88.57 [†]	-0.10	84.13 [†]	+4.55	96.61 [†]	-1.05
	128	32 \times	L1H	SCH	38.42	-8.27	75.99	-10.87	41.75	-16.36	41.66	-17.90	82.88 [†]	-3.23	89.26 [†]	-2.60	94.65 [†]	-1.80	95.87 [†]	-1.74
			L1H	PCH	13.24	-9.58	73.90	-7.38	33.99	-5.79	41.02	-8.93	67.09 [†]	+9.88	88.38 [†]	-0.44	85.26 [†]	+4.46	94.33 [†]	-1.77
			L2H	SCH	36.56	-12.52	83.90	-3.34	47.82	-9.64	49.40	-10.07	75.45 [†]	+3.24	90.75 [†]	-0.89	96.56 [†]	-1.88	97.59 [†]	-0.96
			L2H	PCH	16.59	-6.08	74.31	-4.00	27.86	-3.79	40.86	-6.23	60.16 [†]	+4.13	88.76 [†]	+0.09	84.83 [†]	+5.25	96.33 [†]	-1.33

used unchanged for both datasets. We evaluate two cuts: $\ell=2$ (post-pool₁, $d=1152$) and $\ell=4$ (post-ReLU₂, $d=1024$).

Joint training. For each (dataset, method, ℓ) cell we train for 20 epochs with the upstream optimizer (Adam [26], lr 10^{-3} , AMSGrad, batch 64), using $\mathcal{L}_{CE} + \lambda_{wcc}\mathcal{L}_{WCC}$ on the LightSplit rows (Sec. IV-D). The compression ratios $CR \in \{8, 16, 32\} \times$ fix the bottleneck rank at $k \in \{144, 72, 36\}$ at $\ell=2$ and $k \in \{128, 64, 32\}$ at $\ell=4$.

Foreground mask. MSE and PSNR are computed only over pixels where the ground truth exceeds 0.1; SSIM and LPIPS use a tight bounding-box crop around the same mask, so background pixels (zero in both target and reconstruction) cannot dominate the metric. Whole-image variants are reported in Table XV.

Random-projection sanity check. The LIGHTSPLIT-F reconstruction-resistance plateau depends on the rank of \mathbf{R} ,

not on the specific orthonormal basis. We re-ran $\lambda_{WCC}=10^{-1}$, $CR=8\times$, $\ell=4$ with five additional \mathbf{R} seeds (six runs total). All six agree on the $\ell=4$ plateau ($\times 1.00/\times 1.01$) to within reporting precision; the same saturation is independently witnessed at $\ell=2$ across the in-table $CR \times \lambda_{WCC}$ grid (plateau $\times 1.27/\times 1.09$). Two of the five extra seeds mode-collapse on each dataset (acc. $\leq 12.5\%$); the corresponding rows are listed in Table XV and confirm that mode collapse preserves the rank-induced plateau (identical reconstruction metrics at chance accuracy). Daggered rows in Table XIV are mode-collapse cells from the joint ($\lambda_{WCC}=10^{-1}$, $CR \in \{16, 32\} \times$, $\ell=4$) corner of the grid.

D. FORA: full attack configuration

We adopt the FORA [47] pipeline at the upstream defaults (substitute encoder, residual discriminator with $\lambda_{GP}=1000$,

TABLE X: Label-free backdoor detection F_1 on the backbone output $\bar{\mathbf{r}}$ under LIGHTSPLIT-F and LIGHTSPLIT-L ($\rho=16$). Both variants cross the 3σ flagging threshold at the same ablation cells, so a single F_1 column reports both. The baseline ($\alpha=10^7, n=10, \mu=0.1, p=0.3$) is the mean over 3 seeds; ablation cells are single seeds (one factor changed at a time, others held at baseline). Cells at 0.00 are runs where the malicious client is still the most-anomalous on $\cos(\bar{\mathbf{r}}_i, \bar{\mathbf{r}})$ but its $|z|$ -score does not cross 3σ (cf. Figs. 9, 7). The threshold rule recovers the malicious client across $\alpha \geq 10$ and every n, μ , and $p \leq 0.3$.

Setting	Value(s)	F_1
Baseline (3-seed mean)	$\alpha=10^7, n=10, \mu=0.1, p=0.3$	0.89
α (Dirichlet)	0.1 / 1 / 10	0.00 / 0.00 / 1.00
n (clients)	5 / 20 / 50	1.00 / 0.67 / 1.00
μ (mal. ratio)	0.2 / 0.3	1.00 / 1.00
p (poison rate)	0.1 / 0.2 / 0.5 / 0.8	1.00 / 1.00 / 0.67 / 0.67

TABLE XI: Per-step messages on the cut interface.

Direction	Payload
Forward, C \rightarrow S	$\tilde{\mathbf{z}}_i \in \mathbb{R}^k$
Forward, S \rightarrow C	\mathbf{u}_i (server-backbone output)
Backward, C \rightarrow S	$\partial \mathcal{L}_{\text{CE}} / \partial \mathbf{u}_i$
Backward, S \rightarrow C	$\partial \mathcal{L}_{\text{CE}} / \partial \tilde{\mathbf{z}}_i$

cifar_decoder inversion stack, auxiliary public set, and the MK-MMD objective); the only edit is the insertion of the method object at the released cut.

Per-method k values. The compression sweep $\text{CR}=d/k \in \{8, 16, 32\}$ fixes $k \in \{2048, 1024, 512\}$ on the flat dimension for LIGHTSPLIT-F, and $k_{\text{ch}} \in \{8, 4, 2\}$ for LEARNED 1×1 , which compresses along channels.

Reference decoder. Table XVI additionally reports FORA’s white-box reference decoder, trained directly on the victim’s (\mathbf{z}, \mathbf{x}) pairs. It is non-deployable in U-shaped SL (the server never sees \mathbf{x}) and is included as the leakage ceiling: Δ_{Raw} in Table XVI is computed on this column because it measures information removed from the cut rather than what the deployable surrogate happens to recover.

Pseudo-head pixelwise instability. Pseudo SSIM and PSNR are unreliable: the surrogate-trained decoder drifts in mean RGB (≈ 130 on RAW vs. ≈ 115 at ground truth), which inverts SSIM’s luminance term and produces the negative SSIM cells on RAW and LEARNED 1×1 at $\text{CR}=16 \times$. LPIPS is robust to this drift and is the pseudo-head metric quoted in main-text Table V.

E. Backdoor detection: server-input signal and F_1 table

The main-text Fig. 7 reports the cosine-to-consensus anomaly score on the *server-output* backbone activation $\bar{\mathbf{r}}_i$. For completeness, Fig. 9 shows the same sweep on the *server-input* smashed payload $\tilde{\mathbf{z}}_i$, and Tab. X reports the detection F_1 at the conventional 3σ flagging threshold derived from the same scores. The results are consistent with the main-text claim: both LIGHTSPLIT-F and LIGHTSPLIT-L preserve, and on $\tilde{\mathbf{z}}_i$

TABLE XII: SDAR USL reconstruction sweep on CIFAR-10 across all evaluated split points. USL keeps the classification head on the client, so the SDAR decoder is non-conditional. Rows include raw SDAR, LIGHTSPLIT-F (LS-F) at CR $\{8, 16, 32\}$ with $\lambda_{\text{WCC}} \in \{0, 10^{-2}, 10^{-1}\}$, and learned 1×1 ($L-1 \times 1$) at all CRs.

Level	Method	CR	WCC	MSE \uparrow	SSIM \downarrow	PSNR \downarrow	LPIPS ₂₀ \uparrow
7	Raw	-	-	0.02322	0.57217	16.34	0.4469
7	LS-F	8	0	0.03032	0.35974	15.18	0.5738
7	LS-F	8	0.01	0.07188	0.11824	11.43	0.6338
7	LS-F	8	0.1	0.11004	0.08971	9.58	0.6401
7	LS-F	16	0	0.04993	0.16750	13.02	0.6453
7	LS-F	16	0.01	0.08272	0.09823	10.82	0.6938
7	LS-F	16	0.1	0.08987	0.07650	10.46	0.6791
7	LS-F	32	0	0.09984	0.08373	10.01	0.6845
7	LS-F	32	0.01	0.07421	0.10314	11.30	0.6861
7	LS-F	32	0.1	0.07352	0.12346	11.34	0.6977
7	L-1 \times 1	8	-	0.04894	0.26846	13.10	0.5781
7	L-1 \times 1	16	-	0.04382	0.27357	13.58	0.5623
7	L-1 \times 1	32	-	0.04864	0.20829	13.13	0.5979
4	Raw	-	-	0.00756	0.83230	21.21	0.2899
4	LS-F	8	0	0.01628	0.52442	17.88	0.4677
4	LS-F	8	0.01	0.02629	0.37363	15.80	0.4968
4	LS-F	8	0.1	0.01914	0.52694	17.18	0.5331
4	LS-F	16	0	0.01819	0.46460	17.40	0.4997
4	LS-F	16	0.01	0.02758	0.34383	15.59	0.5315
4	LS-F	16	0.1	0.06923	0.10612	11.60	0.5718
4	LS-F	32	0	0.02425	0.34697	16.15	0.5319
4	LS-F	32	0.01	0.10153	0.05741	9.93	0.6411
4	LS-F	32	0.1	0.14861	-0.04378	8.28	0.6272
4	L-1 \times 1	8	-	0.01849	0.67845	17.33	0.3524
4	L-1 \times 1	16	-	0.01734	0.69247	17.61	0.3621
4	L-1 \times 1	32	-	0.01889	0.66696	17.24	0.4191

amplify, the malicious-client signature relative to RAW. Across the operative regime ($\alpha \geq 10, p \leq 0.3$, every μ , and every n we test) threshold F_1 stays in $[0.67, 1.00]$, reaching 1.0 in most cells. The cells where $F_1 = 0$ are runs in which the malicious client is still the most-anomalous in the field but its $|\text{MAD-}z|$ does not cross the strict 3σ line; the underlying signal, plotted in the figures, remains intact.

F. Lift-back hidden-dim ablation

The MLP lift-back of LIGHTSPLIT-L introduces one server-side hyperparameter not exposed in the main eval, the hidden width m in Eq. (7). Table XVII sweeps m across the four head configurations to motivate the per-dataset values used in the headline runs. Returns are dataset-specific and saturate quickly. The L2H + SCH cell reaches its best at $h=512$ on CIFAR-10 (85.91, -1.33 vs. RAW), $h=2048$ on CIFAR-100 (55.34), $h=128$ on Fashion-MNIST (91.22), and $h=128$ on GTSRB (95.88); larger h stops helping or actively hurts on the easier datasets. The per-dataset hidden dims used in Table IX (cifar10=512, cifar100=2048, fmnist=128, gtsrb=128) are read off this ablation, so the main LIGHTSPLIT-L accuracy is the per-dataset best of this sweep rather than a single fixed h .

G. Training steps and WCC backprop

This appendix walks through one mini-batch of LightSplit training end to end, using the two-optimizer deployment that mirrors how U-shaped split learning is actually run in practice: the client process holds its own optimizer over the head f

TABLE XIII: SDAR VSL reconstruction sweep on CIFAR-10 across all evaluated split points. VSL is the vanilla label-aware split-learning setting from the released SDAR path. Rows include raw SDAR, LIGHTSPLIT-F (LS-F) at CR $\{8, 16, 32\}$ with $\lambda_{WCC} \in \{0, 10^{-2}, 10^{-1}\}$, and learned 1×1 (L-1 \times 1) at all CRs.

Level	Method	CR	WCC	MSE \uparrow	SSIM \downarrow	PSNR \downarrow	LPIPS ₂₀ \uparrow
7	Raw	-	-	0.02192	0.56531	16.59	0.4415
7	LS-F	8	0	0.03217	0.34231	14.93	0.5485
7	LS-F	8	0.01	0.03932	0.25308	14.05	0.5904
7	LS-F	8	0.1	0.07484	0.10033	11.26	0.6545
7	LS-F	16	0	0.02941	0.32989	15.31	0.5868
7	LS-F	16	0.01	0.04610	0.19922	13.36	0.6172
7	LS-F	16	0.1	0.06222	0.12384	12.06	0.6214
7	LS-F	32	0	0.03770	0.24993	14.24	0.6000
7	LS-F	32	0.01	0.05000	0.18094	13.01	0.6254
7	LS-F	32	0.1	0.07324	0.10886	11.35	0.6373
7	L-1 \times 1	8	-	0.03162	0.40975	15.00	0.5247
7	L-1 \times 1	16	-	0.03874	0.33962	14.12	0.5453
7	L-1 \times 1	32	-	0.04749	0.25197	13.23	0.5969
4	Raw	-	-	0.00897	0.79435	20.47	0.2811
4	LS-F	8	0	0.01699	0.49547	17.70	0.4770
4	LS-F	8	0.01	0.01949	0.51908	17.10	0.4744
4	LS-F	8	0.1	0.10127	0.08058	9.95	0.5889
4	LS-F	16	0	0.02021	0.42459	16.94	0.5006
4	LS-F	16	0.01	0.08546	0.12062	10.68	0.5660
4	LS-F	16	0.1	0.09484	0.07475	10.23	0.6018
4	LS-F	32	0	0.02272	0.38212	16.44	0.5293
4	LS-F	32	0.01	0.03501	0.24040	14.56	0.5405
4	LS-F	32	0.1	0.04189	0.23421	13.78	0.5534
4	L-1 \times 1	8	-	0.01689	0.68547	17.72	0.3651
4	L-1 \times 1	16	-	0.02329	0.65029	16.33	0.3732
4	L-1 \times 1	32	-	0.01980	0.65484	17.03	0.4010

and the tail h , and the server process holds its own optimizer over the backbone g and, in LIGHTSPLIT-L, the learned lift-back ϕ . The projection matrix \mathbf{R} is fixed at provisioning time and is never touched by either optimizer. We provide this walkthrough as a self-contained reference for the forward and backward computations, the messages exchanged across the trust boundary, and the parameter updates each side applies. A useful by-product of laying everything out in this form is that it makes immediate the claim, stated in the methodology, that adding \mathcal{L}_{WCC} leaves the client-server protocol of plain U-shaped split learning unchanged: the forward and backward payloads exchanged at the cut, and the server’s parameter update, are bit-identical with or without \mathcal{L}_{WCC} .

1) *Computational complexity*: Let b denote the mini-batch size, let the cut activation have shape $C \times H \times W$ and flattened dimension $d = CHW$, let k be the transmitted width ($CR = d/k$), and let m be the hidden width of the learned lift-back. We count only the bottleneck and lift-back overhead beyond the common split model $h \circ g \circ f$.

a) *Cost of LightSplit*: Both LIGHTSPLIT variants send exactly bk scalars per batch. In LIGHTSPLIT-F, the client computes the fixed projection $\mathbf{R}^\top \mathbf{z}$ and the server applies the fixed lift-back $\mathbf{R}\tilde{\mathbf{z}}$, so the extra work is $O(bdk)$ on each side and the bottleneck adds no trainable parameters. LIGHTSPLIT-L keeps the same client computation and the same bk communication, but replaces the fixed server lift-back with the MLP $k \rightarrow m \rightarrow d$. Its extra adaptation cost is therefore server-side: $O(m(k+d))$ trainable parameters and $O(bm(k+d))$ work. WCC, when enabled, is only a training-

SDAR USL reconstructions, level 4, CR=8

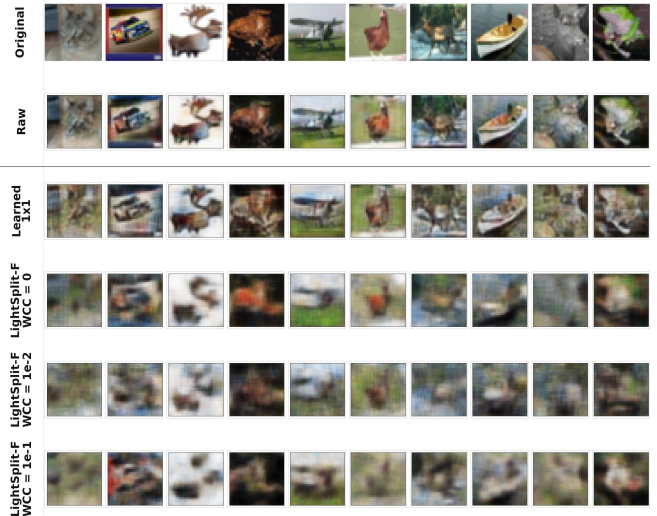


Fig. 10: SDAR level-4 USL reconstructions on CIFAR-10 at CR=8. Rows compare original images against raw SDAR, LEARNED 1×1 , and LIGHTSPLIT-F with WCC strengths 0, 10^{-2} , and 10^{-1} .

SDAR USL reconstructions, level 4, CR=16

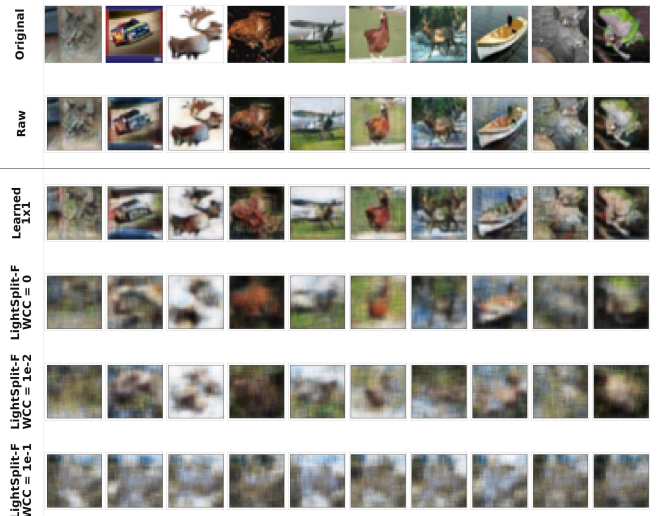


Fig. 11: Level-4 USL, CR=16; same layout as Fig. 10.

time client regularizer on $\tilde{\mathbf{z}}$; it costs $O(bk)$ arithmetic, sends no extra values, and disappears at inference.

2) *Forward pass*:

a) *Step 1 (client, head)*: On a mini-batch $\{(\mathbf{x}_i, \mathbf{y}_i)\}_{i=1}^b$, the client computes the cut-layer activation $\mathbf{z}_i = f(\mathbf{x}_i) \in \mathbb{R}^d$.

b) *Step 2 (client, projection)*: The client applies the fixed projection $\tilde{\mathbf{z}}_i = \mathbf{R}^\top \mathbf{z}_i \in \mathbb{R}^k$, following Eq. (2). The resulting tensor is recorded in the client’s autograd graph as a function of f ’s parameters.

c) *Step 3 (network, client \rightarrow server)*: The client transmits $\{\tilde{\mathbf{z}}_i\}_{i=1}^b$ to the server. This is the only forward payload

TABLE XIV: Full UnSplit sweep on MnistNet. Foreground-masked reconstruction metric $\text{MSE}_{\text{fg}}/\text{Raw}$ (larger = stronger reconstruction resistance; values < 1 leak more than RAW) and victim test accuracy across the two UnSplit cut depths and three compression ratios. The split-2 cut is shallow enough that RAW recovers visible structure, so the per-method ratio is informative. At split-4 even RAW reconstructions are mostly degraded (foreground $\text{MSE} \sim 0.70$), so split-4 ratios are dominated by the baseline rather than the method; we still report them for completeness. Rows marked \dagger are mode-collapsed runs (test accuracy $\leq 12\%$): the model failed to learn under the combined CR/WCC pressure at split-4, so the $\times 1.00$ ratio reflects identical degenerate reconstructions on both sides rather than a reduction in leakage. The seed sweep at $\lambda_{\text{WCC}}=10^{-1}$, CR=8 \times , split-4 (five additional R seeds; rows appear in Table XV) reproduces the split-4 plateau bit-identically; the split-2 plateau ($\times 1.27/\times 1.09$) is independently saturated across the CR and λ_{WCC} sweep within the present table. Whole-image variants of every cell are reported in Table XV.

Method	Split	λ_{WCC}	CR	MNIST		Fashion-MNIST	
				Acc. (%)	$\text{MSE}_{\text{fg}}/\text{Raw} \uparrow$	Acc. (%)	$\text{MSE}_{\text{fg}}/\text{Raw} \uparrow$
<i>Cut at split layer 2 (MnistNet post-pool₁, d=1152).</i>							
RAW	2	–	1 \times	99.0	$\times 1.00$	88.6	$\times 1.00$
LEARNED 1 \times 1	2	–	8 \times	98.7	$\times 1.03$	87.9	$\times 1.06$
LEARNED 1 \times 1	2	–	16 \times	98.6	$\times 0.97$	88.6	$\times 1.08$
LEARNED 1 \times 1	2	–	32 \times	99.0	$\times 1.08$	88.5	$\times 0.93$
LIGHTSPLIT-F	2	0	8 \times	98.0	$\times 1.27$	89.0	$\times 1.09$
LIGHTSPLIT-F	2	0	16 \times	97.7	$\times 1.27$	87.0	$\times 1.09$
LIGHTSPLIT-F	2	0	32 \times	97.6	$\times 1.27$	84.0	$\times 1.08$
LIGHTSPLIT-F	2	10^{-2}	8 \times	97.5	$\times 1.27$	86.1	$\times 1.09$
LIGHTSPLIT-F	2	10^{-2}	16 \times	97.5	$\times 1.27$	85.8	$\times 1.09$
LIGHTSPLIT-F	2	10^{-2}	32 \times	95.9	$\times 1.27$	86.0	$\times 1.09$
LIGHTSPLIT-F	2	10^{-1}	8 \times	97.2	$\times 1.27$	84.7	$\times 1.09$
LIGHTSPLIT-F	2	10^{-1}	16 \times	97.0	$\times 1.27$	85.8	$\times 1.09$
LIGHTSPLIT-F	2	10^{-1}	32 \times	96.7	$\times 1.27$	84.1	$\times 1.09$
<i>Cut at split layer 4 (MnistNet post-ReLU₂, d=1024).</i>							
RAW	4	–	1 \times	99.0	$\times 1.00$	88.8	$\times 1.00$
LEARNED 1 \times 1	4	–	8 \times	98.6	$\times 0.82$	88.4	$\times 0.97$
LEARNED 1 \times 1	4	–	16 \times	97.5	$\times 0.91$	88.1	$\times 0.98$
LEARNED 1 \times 1	4	–	32 \times	98.3	$\times 0.85$	88.7	$\times 0.94$
LIGHTSPLIT-F	4	0	8 \times	98.3	$\times 0.89$	89.0	$\times 1.01$
LIGHTSPLIT-F	4	0	16 \times	98.2	$\times 0.97$	87.1	$\times 1.01$
LIGHTSPLIT-F	4	0	32 \times	98.6	$\times 1.00$	87.0	$\times 1.01$
LIGHTSPLIT-F	4	10^{-2}	8 \times	98.3	$\times 1.00$	87.8	$\times 1.01$
LIGHTSPLIT-F	4	10^{-2}	16 \times	98.7	$\times 1.00$	86.9	$\times 1.01$
LIGHTSPLIT-F	4	10^{-2}	32 \times	97.0	$\times 1.00$	84.8	$\times 1.01$
LIGHTSPLIT-F	4	10^{-1}	8 \times	97.0	$\times 1.00$	86.1	$\times 1.01$
LIGHTSPLIT-F	4	10^{-1}	16 \times	11.3 \dagger	$\times 1.00$	84.5	$\times 1.01$
LIGHTSPLIT-F	4	10^{-1}	32 \times	10.2 \dagger	$\times 1.00$	85.1	$\times 1.01$

that crosses the trust boundary; the labels $\{y_i\}$ remain on the client.

d) *Step 4 (server, lift-back)*: The server computes $\hat{z}_i = \phi(\tilde{z}_i)$, where ϕ is either the fixed map of LIGHTSPLIT-F or the learned MLP of LIGHTSPLIT-L. The result is recorded in the server’s autograd graph, which is a graph distinct from the client’s.

e) *Step 5 (server, backbone)*: The server computes $\mathbf{u}_i = g(\hat{z}_i)$ and retains the server-side autograd graph rooted at \tilde{z}_i .

f) *Step 6 (network, server \rightarrow client)*: The server transmits $\{\mathbf{u}_i\}_{i=1}^b$ to the client. On reception, the client treats \mathbf{u}_i as a fresh leaf with `requires_grad=True`; the client’s autograd graph resumes from \mathbf{u}_i onward.

g) *Step 7 (client, tail)*.: The client computes $\hat{y}_i = h(\mathbf{u}_i)$.

h) *Step 8 (client, cross-entropy loss)*: The client evaluates the per-batch cross-entropy $\mathcal{L}_{\text{CE}} = b^{-1} \sum_i \ell_{\text{CE}}(\hat{y}_i, y_i)$. By construction, \mathcal{L}_{CE} depends on h , \mathbf{u} , and y in the client’s graph, but not on \tilde{z} directly.

i) *Step 9 (client, within-class compaction)*: Reusing the \tilde{z}_i tensors from Step 2, which remain alive in the client’s autograd graph, the client computes \mathcal{L}_{WCC} from Eq. (10). The labels y are used only to partition the batch into per-class index sets S_c , in keeping with the U-shaped topology in which labels never leave the client.

j) *Step 10 (client, total loss)*: The client forms the scalar objective $\mathcal{L} = \mathcal{L}_{\text{CE}} + \lambda_{\text{WCC}} \mathcal{L}_{\text{WCC}}$ as in Eq. (11).

3) *Backward pass: client (Phase 1)*:

a) *Step 11*: The client zeros its optimizer state with `client_optimizer.zero_grad()`.

b) *Step 12*.: The client invokes `loss.backward()` on its local graph. Autograd traverses the two branches simultaneously:

- The CE branch reaches h and accumulates $\partial \mathcal{L}_{\text{CE}} / \partial \theta_h$ into h ’s `.grad`, then propagates back to \mathbf{u} , leaving $\partial \mathcal{L}_{\text{CE}} / \partial \mathbf{u}$ on \mathbf{u} ’s `.grad`. Because \mathbf{u} is a leaf in the client’s graph, traversal stops there.

SDAR USL reconstructions, level 4, CR=32

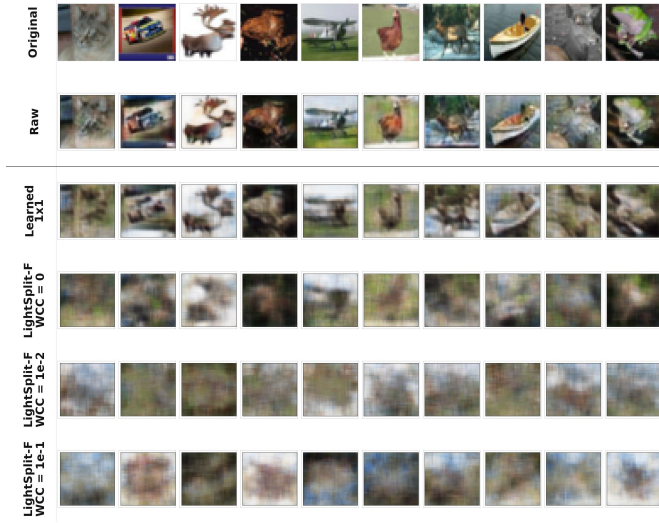


Fig. 12: Level-4 USL, CR=32; same layout as Fig. 10.

SDAR VSL reconstructions, level 4, CR=16

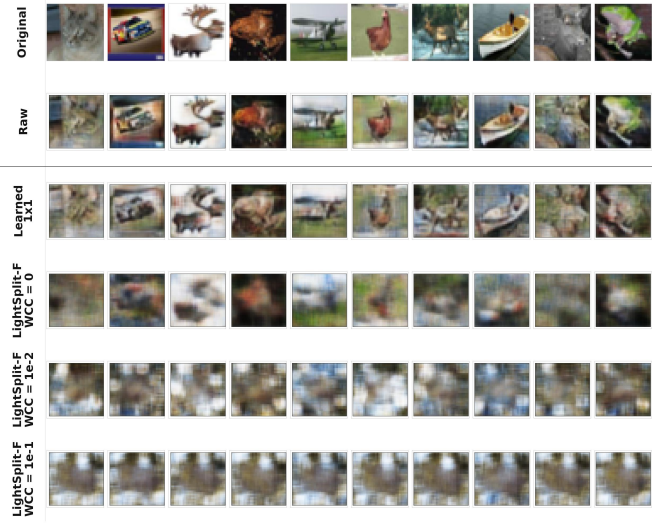


Fig. 14: Level-4 VSL, CR=16; same layout as Fig. 10.

SDAR VSL reconstructions, level 4, CR=8

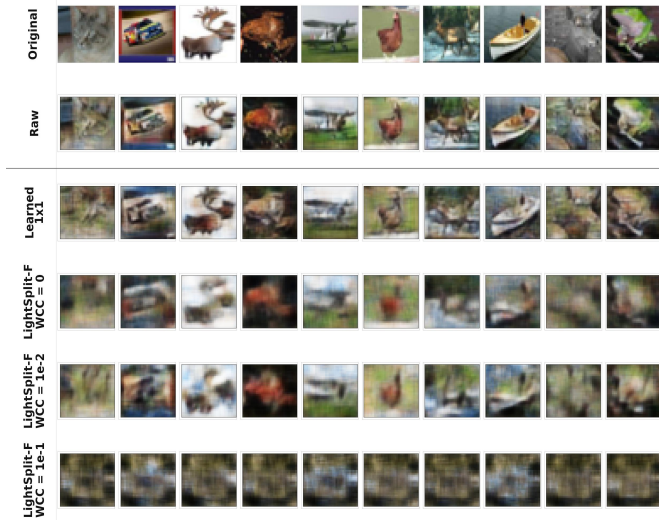


Fig. 13: Level-4 VSL, CR=8; same layout as Fig. 10.

SDAR VSL reconstructions, level 4, CR=32

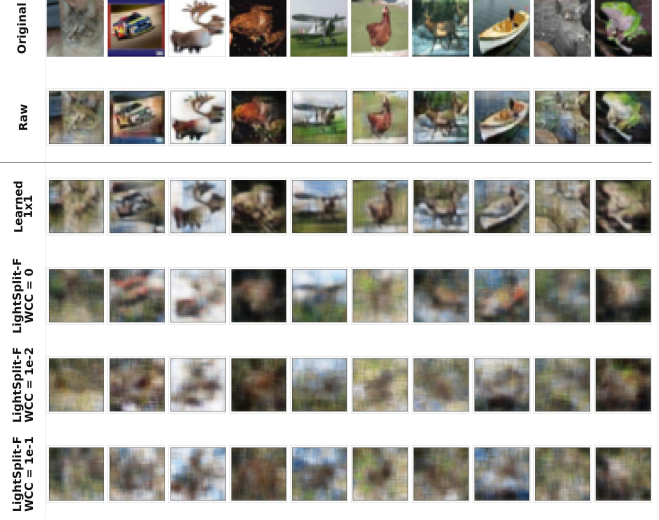


Fig. 15: Level-4 VSL, CR=32; same layout as Fig. 10.

- The WCC branch propagates from \mathcal{L}_{WCC} through \tilde{z} and the fixed factor \mathbf{R}^\top to f , accumulating $\lambda_{WCC} \partial \mathcal{L}_{WCC} / \partial \theta_f$ into f 's `.grad`, and leaving $\lambda_{WCC} \partial \mathcal{L}_{WCC} / \partial \tilde{z}$ on \tilde{z} 's `.grad`.

At this point f 's `.grad` contains only the contribution from the client-local term; the contribution from \mathcal{L}_{CE} requires the server's backward signal, which has not yet arrived.

c) *Step 13 (network, client \rightarrow server):* The client transmits $\partial \mathcal{L}_{CE} / \partial \mathbf{u}$ to the server. This is the standard backward payload of U-shaped split learning.

4) *Backward pass: server:*

a) *Step 14:* The server zeros its optimizer state with `server_optimizer.zero_grad()`.

b) *Step 15:* The server uses the incoming $\partial \mathcal{L}_{CE} / \partial \mathbf{u}$ as the upstream seed and calls `u.backward(grad_output)` on its server-side graph. Autograd traverses $\mathbf{u} \rightarrow g \rightarrow \hat{z} \rightarrow \phi \rightarrow \tilde{z}$, accumulating $\partial \mathcal{L}_{CE} / \partial \theta_g$ and (in LIGHTSPLIT-L) $\partial \mathcal{L}_{CE} / \partial \theta_\phi$ into the corresponding `.grad` buffers, and leaving $\partial \mathcal{L}_{CE} / \partial \tilde{z}$ on the server-side \tilde{z} .

c) *Step 16:* The server applies `server_optimizer.step()`. The update of θ_g and θ_ϕ is determined entirely by \mathcal{L}_{CE} .

d) *Step 17 (network, server \rightarrow client):* The server transmits $\partial \mathcal{L}_{CE} / \partial \tilde{z}$ back to the client.

5) *Backward pass: client (Phase 2):*

a) *Step 18:* The client receives $\partial \mathcal{L}_{CE} / \partial \tilde{z}$ and adds it to the contribution already sitting on \tilde{z} 's `.grad` from Step 12,

SDAR USL reconstructions, level 7, CR=8

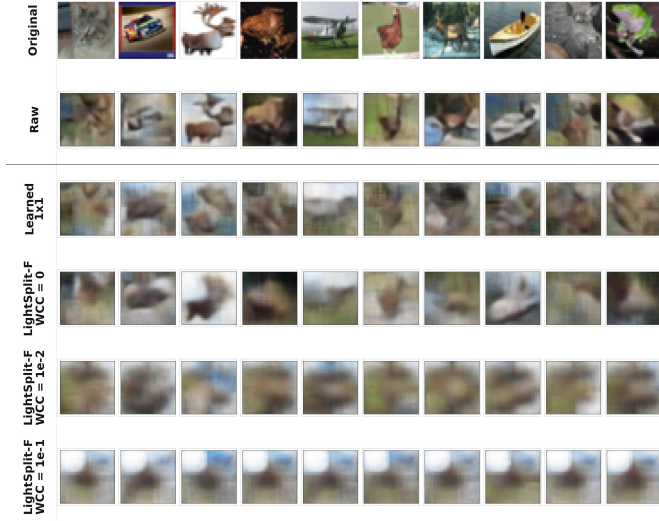


Fig. 16: Level-7 USL, CR=8; same layout as Fig. 10.

SDAR USL reconstructions, level 7, CR=32

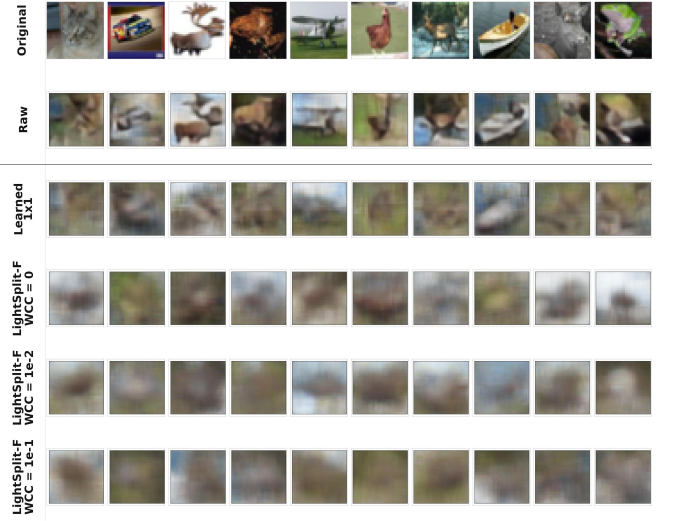


Fig. 18: Level-7 USL, CR=32; same layout as Fig. 10.

SDAR USL reconstructions, level 7, CR=16

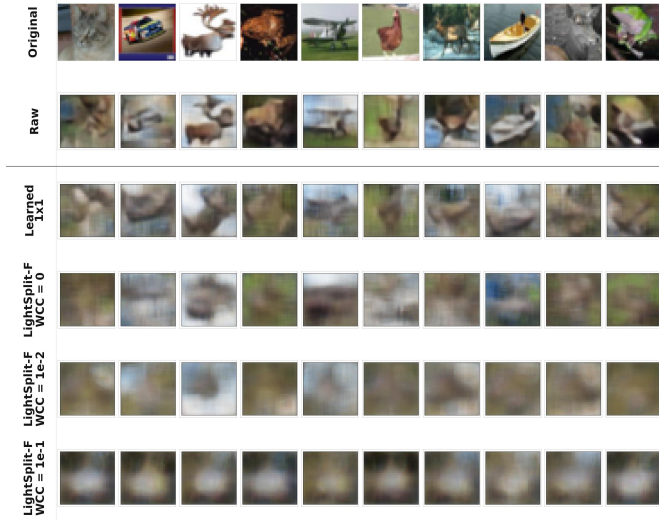


Fig. 17: Level-7 USL, CR=16; same layout as Fig. 10.

SDAR VSL reconstructions, level 7, CR=8

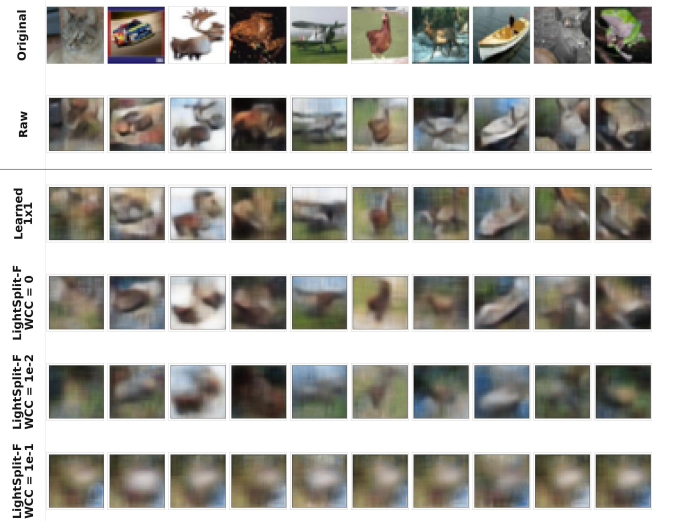


Fig. 19: Level-7 VSL, CR=8; same layout as Fig. 10.

yielding

$$\frac{\partial \mathcal{L}}{\partial \tilde{\mathbf{z}}} = \frac{\partial \mathcal{L}_{\text{CE}}}{\partial \tilde{\mathbf{z}}} + \lambda_{\text{WCC}} \frac{\partial \mathcal{L}_{\text{WCC}}}{\partial \tilde{\mathbf{z}}}. \quad (12)$$

This client-local addition is the only point in the entire training step at which the two gradient pathways meet.

b) Step 19.: The client backpropagates Eq. (12) through the fixed projection (chain-rule by \mathbf{R} , which has no parameters to update) and through f . The CE contribution to f 's gradient is now accumulated on top of the WCC contribution from Step 12, giving

$$\frac{\partial \mathcal{L}}{\partial \theta_f} = \frac{\partial \mathcal{L}_{\text{CE}}}{\partial \theta_f} + \lambda_{\text{WCC}} \frac{\partial \mathcal{L}_{\text{WCC}}}{\partial \theta_f}. \quad (13)$$

c) Step 20.: The client applies `client_optimizer.step()`, updating h from $\partial \mathcal{L}_{\text{CE}} / \partial \theta_h$ and f from Eq. (13). The current mini-batch step is complete.

6) Wire-level and optimizer-level summary: The four messages exchanged at the cut interface during a single mini-batch step are summarized in Table XI: the forward payload $\tilde{\mathbf{z}}$, the server's return signal \mathbf{u} , and the two backward gradient signals $\partial \mathcal{L}_{\text{CE}} / \partial \mathbf{u}$ and $\partial \mathcal{L}_{\text{CE}} / \partial \tilde{\mathbf{z}}$. Each direction transmits exactly one tensor per sample. The server's update of (θ_g, θ_ϕ) depends on \mathcal{L}_{CE} alone, because \mathcal{L}_{WCC} has no functional dependency on any server-side variable. The client's update of θ_h depends on \mathcal{L}_{CE} alone for the same reason, and the client's update of θ_f

SDAR VSL reconstructions, level 7, CR=16

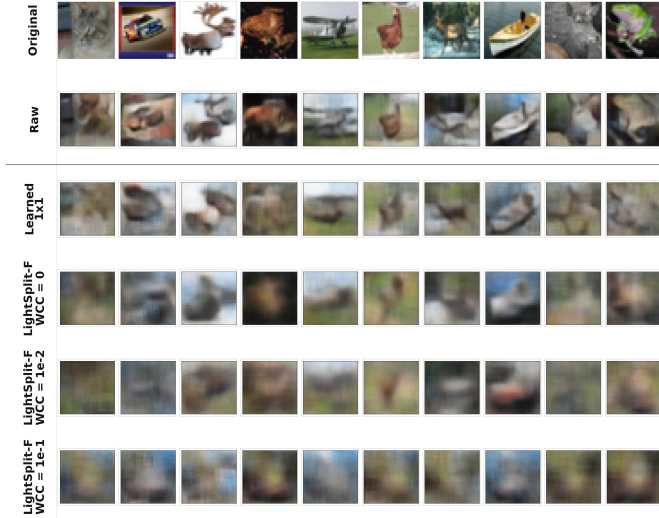


Fig. 20: Level-7 VSL, CR=16; same layout as Fig. 10.

SDAR VSL reconstructions, level 7, CR=32

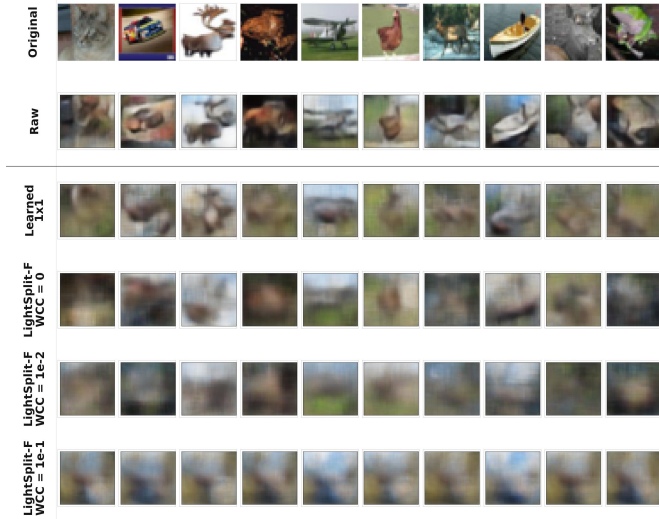


Fig. 21: Level-7 VSL, CR=32; same layout as Fig. 10.

is the sum of contributions from \mathcal{L}_{CE} and \mathcal{L}_{WCC} (the latter being a client-local quantity). \mathbf{R} is fixed and never updated.

A direct consequence is that the protocol described in Steps 1 to 20 reduces to the standard U-shaped split-learning protocol when $\lambda_{WCC} = 0$, with neither the cut-layer messages nor the server-side update changing form. Setting $\lambda_{WCC} > 0$ introduces the additive client-local term in Eq. (13) and nothing else.

7) *Equivalence between single- and two-optimizer implementations:* For any first-order optimizer (SGD, Adam, AdamW, etc.) applied parameter-wise, splitting a single `loss.backward()` / `optimizer.step()` call into two independent (`zero_grad`, `backward`, `step`) se-

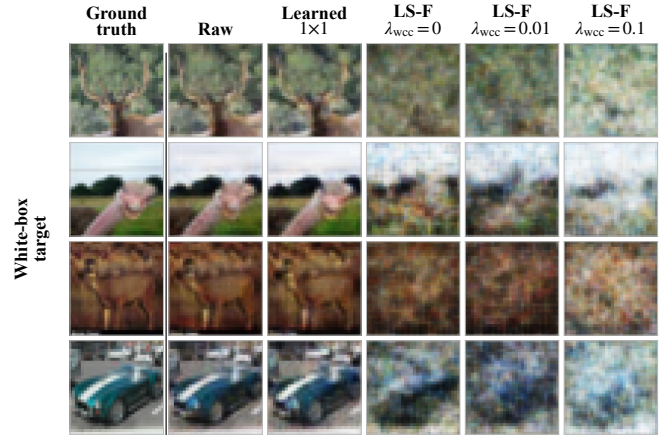


Fig. 22: FORA white-box reference-decoder reconstructions on CIFAR-10 at CR=8x. Each row is one sample; columns are Ground truth followed by each method.

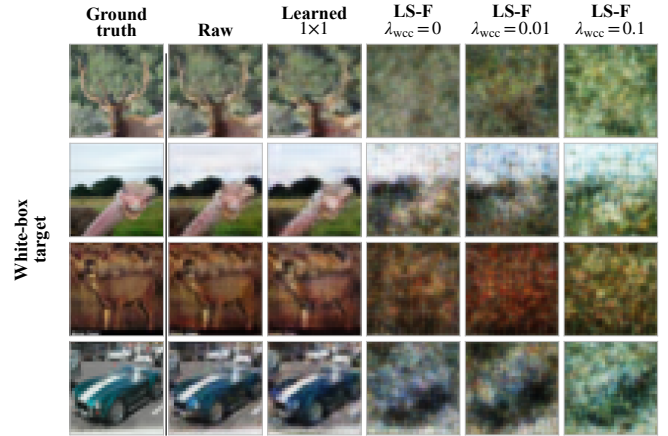


Fig. 23: FORA white-box reference-decoder reconstructions on CIFAR-10 at CR=16x.

quences, one on each side of the cut, produces identical per-parameter updates. The reason is that parameter-wise optimizers depend only on each parameter’s accumulated gradient, which is determined by the autograd graph rather than by the process boundary. Our reference implementations in Alg. 2 and Alg. 1 express the procedure with one optimizer per side; the two-optimizer deployment described above produces mathematically identical f , h , g , and ϕ updates.

8) *Compact derivation in equations:* For a reader who prefers the gradient bookkeeping in equation form, this subsection restates the per-step computation as a sequence of derivatives. Let $\theta_f, \theta_h, \theta_g, \theta_\phi$ denote the trainable parameters of f, h, g, ϕ , respectively, and let J_F denote the Jacobian of a map F at the current point.

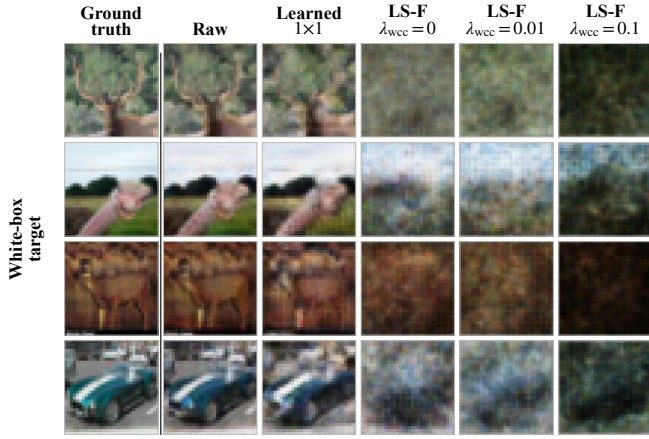


Fig. 24: FORA white-box reference-decoder reconstructions on CIFAR-10 at CR=32 \times .

a) *Forward composition:* Per sample i in a batch of size b :

$$\mathbf{z}_i = f(\mathbf{x}_i; \theta_f), \quad (14)$$

$$\tilde{\mathbf{z}}_i = \mathbf{R}^\top \mathbf{z}_i, \quad (15)$$

$$\hat{\mathbf{z}}_i = \phi(\tilde{\mathbf{z}}_i; \theta_\phi), \quad (16)$$

$$\mathbf{u}_i = g(\hat{\mathbf{z}}_i; \theta_g), \quad (17)$$

$$\hat{y}_i = h(\mathbf{u}_i; \theta_h). \quad (18)$$

b) *Losses:*

$$\mathcal{L}_{\text{CE}} = \frac{1}{b} \sum_{i=1}^b \ell_{\text{CE}}(\hat{y}_i, y_i), \quad (19)$$

$$\mathcal{L}_{\text{WCC}} = \sum_{c \in \mathcal{Y}_b} \frac{1}{|\mathcal{S}_c|} \sum_{i \in \mathcal{S}_c} \|\tilde{\mathbf{z}}_i - \boldsymbol{\mu}_c\|_2^2, \quad (20)$$

$$\mathcal{L} = \mathcal{L}_{\text{CE}} + \lambda_{\text{WCC}} \mathcal{L}_{\text{WCC}}. \quad (21)$$

c) *Functional dependencies:* \mathcal{L}_{CE} depends on $\tilde{\mathbf{z}}_i$ only through the round-trip $\tilde{\mathbf{z}}_i \rightarrow \hat{\mathbf{z}}_i \rightarrow \mathbf{u}_i \rightarrow \hat{y}_i$. \mathcal{L}_{WCC} depends on $\{\tilde{\mathbf{z}}_i, y_i\}$ alone, so its partials with respect to all server-side variables vanish:

$$\begin{aligned} \frac{\partial \mathcal{L}_{\text{WCC}}}{\partial \mathbf{u}_i} &= \frac{\partial \mathcal{L}_{\text{WCC}}}{\partial \hat{\mathbf{z}}_i} = \frac{\partial \mathcal{L}_{\text{WCC}}}{\partial \theta_h} \\ &= \frac{\partial \mathcal{L}_{\text{WCC}}}{\partial \theta_g} = \frac{\partial \mathcal{L}_{\text{WCC}}}{\partial \theta_\phi} = \mathbf{0}. \end{aligned} \quad (22)$$

d) *Backward, client phase 1:* Starting from \mathcal{L} and walking back through the client's autograd graph until the cut interface:

$$\frac{\partial \mathcal{L}}{\partial \hat{y}_i} = \frac{\partial \mathcal{L}_{\text{CE}}}{\partial \hat{y}_i}, \quad (23)$$

$$\frac{\partial \mathcal{L}}{\partial \theta_h} = \sum_i \frac{\partial \mathcal{L}_{\text{CE}}}{\partial \hat{y}_i} J_h(\mathbf{u}_i; \theta_h)_{\theta_h}, \quad (24)$$

$$\frac{\partial \mathcal{L}}{\partial \mathbf{u}_i} = \frac{\partial \mathcal{L}_{\text{CE}}}{\partial \hat{y}_i} J_h(\mathbf{u}_i; \theta_h)_{\mathbf{u}_i}. \quad (25)$$

The CE gradient at \mathbf{u}_i in Eq. (25) is the only quantity transmitted from client to server in the backward direction. By Eq. (22), this quantity is independent of \mathcal{L}_{WCC} .

In parallel, autograd accumulates the WCC contribution along the head-side chain:

$$\frac{\partial \mathcal{L}_{\text{WCC}}}{\partial \tilde{\mathbf{z}}_i} \quad (\text{closed form from Eq. (20)}), \quad (26)$$

$$\frac{\partial \mathcal{L}_{\text{WCC}}}{\partial \mathbf{z}_i} = \mathbf{R} \frac{\partial \mathcal{L}_{\text{WCC}}}{\partial \tilde{\mathbf{z}}_i}, \quad (27)$$

$$\frac{\partial \mathcal{L}_{\text{WCC}}}{\partial \theta_f} = \sum_i \frac{\partial \mathcal{L}_{\text{WCC}}}{\partial \mathbf{z}_i} J_f(\mathbf{x}_i; \theta_f)_{\theta_f}. \quad (28)$$

e) *Backward, server:* The server seeds its backward with the incoming $\partial \mathcal{L}_{\text{CE}} / \partial \mathbf{u}_i$ from Eq. (25) and produces:

$$\frac{\partial \mathcal{L}_{\text{CE}}}{\partial \theta_g} = \sum_i \frac{\partial \mathcal{L}_{\text{CE}}}{\partial \mathbf{u}_i} J_g(\hat{\mathbf{z}}_i; \theta_g)_{\theta_g}, \quad (29)$$

$$\frac{\partial \mathcal{L}_{\text{CE}}}{\partial \hat{\mathbf{z}}_i} = \frac{\partial \mathcal{L}_{\text{CE}}}{\partial \mathbf{u}_i} J_g(\hat{\mathbf{z}}_i; \theta_g)_{\hat{\mathbf{z}}_i}, \quad (30)$$

$$\frac{\partial \mathcal{L}_{\text{CE}}}{\partial \theta_\phi} = \sum_i \frac{\partial \mathcal{L}_{\text{CE}}}{\partial \hat{\mathbf{z}}_i} J_\phi(\tilde{\mathbf{z}}_i; \theta_\phi)_{\theta_\phi}, \quad (31)$$

$$\frac{\partial \mathcal{L}_{\text{CE}}}{\partial \tilde{\mathbf{z}}_i} = \frac{\partial \mathcal{L}_{\text{CE}}}{\partial \hat{\mathbf{z}}_i} J_\phi(\tilde{\mathbf{z}}_i; \theta_\phi)_{\tilde{\mathbf{z}}_i}. \quad (32)$$

By Eq. (22), Eqs. (29) to (31) are also the gradients of \mathcal{L} with respect to the server-side parameters, not just of \mathcal{L}_{CE} . Eq. (32) is the only quantity transmitted from server to client in the backward direction.

f) *Backward, client phase 2 (gradient fusion):* The client adds the server's contribution from Eq. (32) to the WCC contribution from Eq. (26):

$$\frac{\partial \mathcal{L}}{\partial \tilde{\mathbf{z}}_i} = \frac{\partial \mathcal{L}_{\text{CE}}}{\partial \tilde{\mathbf{z}}_i} + \lambda_{\text{WCC}} \frac{\partial \mathcal{L}_{\text{WCC}}}{\partial \tilde{\mathbf{z}}_i}. \quad (33)$$

This is the unique addition step at which CE and WCC information meet, and it occurs entirely on the client. Continuing through the projection and the head:

$$\frac{\partial \mathcal{L}}{\partial \mathbf{z}_i} = \mathbf{R} \frac{\partial \mathcal{L}}{\partial \tilde{\mathbf{z}}_i}, \quad (34)$$

$$\frac{\partial \mathcal{L}}{\partial \theta_f} = \sum_i \frac{\partial \mathcal{L}}{\partial \mathbf{z}_i} J_f(\mathbf{x}_i; \theta_f)_{\theta_f} = \frac{\partial \mathcal{L}_{\text{CE}}}{\partial \theta_f} + \lambda_{\text{WCC}} \frac{\partial \mathcal{L}_{\text{WCC}}}{\partial \theta_f}. \quad (35)$$

g) *Optimizer updates:* Writing η for the learning rate and using SGD for brevity (any parameter-wise first-order rule applies analogously, with its own state):

$$\text{(server)} \quad \theta_g \leftarrow \theta_g - \eta \frac{\partial \mathcal{L}_{\text{CE}}}{\partial \theta_g}, \quad (36)$$

$$\theta_\phi \leftarrow \theta_\phi - \eta \frac{\partial \mathcal{L}_{\text{CE}}}{\partial \theta_\phi} \quad (\text{LIGHTSPLIT-L only}), \quad (37)$$

$$\text{(client)} \quad \theta_h \leftarrow \theta_h - \eta \frac{\partial \mathcal{L}_{\text{CE}}}{\partial \theta_h}, \quad (38)$$

$$\theta_f \leftarrow \theta_f - \eta \left(\frac{\partial \mathcal{L}_{\text{CE}}}{\partial \theta_f} + \lambda_{\text{WCC}} \frac{\partial \mathcal{L}_{\text{WCC}}}{\partial \theta_f} \right). \quad (39)$$

The matrix \mathbf{R} is treated as a fixed constant and receives no update.

h) Reduction to plain U-shaped split learning: The cut-interface payloads $\tilde{\mathbf{z}}_i$ in Eq. (15), \mathbf{u}_i in Eq. (17), $\partial\mathcal{L}_{\text{CE}}/\partial\mathbf{u}_i$ in Eq. (25), and $\partial\mathcal{L}_{\text{CE}}/\partial\tilde{\mathbf{z}}_i$ in Eq. (32) are functions of \mathcal{L}_{CE} and the model alone. Likewise, the server's update rules Eqs. (36) and (37) and the client's tail update Eq. (38) are functions of \mathcal{L}_{CE} alone. Setting $\lambda_{\text{WCC}} = 0$ in Eq. (39) thus recovers exactly the protocol of plain U-shaped split learning. The additive WCC term in Eq. (39) is the sole point at which the two regimes differ, and that term is computed and applied entirely on the client.

TABLE XV: UnSplit reconstruction metrics (**whole-image**): each metric is computed over all 28×28 pixels of the reconstructed image and target. Δ_{Raw} is the metric ratio relative to the per-(dataset, split) RAW baseline. At $\lambda_{\text{wcc}}=10^{-1}$, split-4, CR=8 \times we list the original run plus five additional **R** seeds; rows with identical reconstruction metrics but varying victim accuracy are seed replicas (collapsed accuracies $\leq 12.5\%$ are mode-collapsed seeds, the rest are healthy).

Dataset	Method	Split	k	CR	Acc. (%)	MSE \uparrow	Δ_{Raw}	SSIM \downarrow	PSNR \downarrow	LPIPS \uparrow
MNIST	RAW	2	-	-	99.02	0.1323	$\times 1.00$	0.1798	8.85	0.4540
MNIST	LEARNED 1×1	2	144	8 \times	98.65	0.1352	$\times 1.02$	0.0763	8.69	0.4792
MNIST	LEARNED 1×1	2	72	16 \times	98.60	0.1262	$\times 0.95$	0.1819	8.99	0.4450
MNIST	LEARNED 1×1	2	36	32 \times	98.95	0.1406	$\times 1.06$	0.1546	8.52	0.5309
MNIST	LIGHTSPLIT-F ($\lambda_{\text{WCC}}=0$)	2	144	8 \times	97.95	0.1660	$\times 1.25$	0.1281	7.82	0.6811
MNIST	LIGHTSPLIT-F ($\lambda_{\text{WCC}}=10^{-2}$)	2	144	8 \times	97.50	0.1656	$\times 1.25$	0.1278	7.81	0.6813
MNIST	LIGHTSPLIT-F ($\lambda_{\text{WCC}}=10^{-1}$)	2	144	8 \times	97.20	0.1656	$\times 1.25$	0.1278	7.81	0.6813
MNIST	LIGHTSPLIT-F ($\lambda_{\text{WCC}}=0$)	2	72	16 \times	97.66	0.1669	$\times 1.26$	0.1278	7.81	0.6815
MNIST	LIGHTSPLIT-F ($\lambda_{\text{WCC}}=10^{-2}$)	2	72	16 \times	97.46	0.1656	$\times 1.25$	0.1278	7.81	0.6813
MNIST	LIGHTSPLIT-F ($\lambda_{\text{WCC}}=10^{-1}$)	2	72	16 \times	96.95	0.1656	$\times 1.25$	0.1278	7.81	0.6813
MNIST	LIGHTSPLIT-F ($\lambda_{\text{WCC}}=0$)	2	36	32 \times	97.56	0.1759	$\times 1.33$	0.1045	7.83	0.6954
MNIST	LIGHTSPLIT-F ($\lambda_{\text{WCC}}=10^{-2}$)	2	36	32 \times	95.90	0.1656	$\times 1.25$	0.1278	7.81	0.6813
MNIST	LIGHTSPLIT-F ($\lambda_{\text{WCC}}=10^{-1}$)	2	36	32 \times	96.65	0.1656	$\times 1.25$	0.1278	7.81	0.6813
MNIST	RAW	4	-	-	98.96	0.1771	$\times 1.00$	0.0892	7.81	0.5702
MNIST	LEARNED 1×1	4	128	8 \times	98.60	0.1466	$\times 0.83$	0.0448	8.50	0.4397
MNIST	LEARNED 1×1	4	64	16 \times	97.45	0.1621	$\times 0.92$	0.0657	8.18	0.5142
MNIST	LEARNED 1×1	4	32	32 \times	98.25	0.1529	$\times 0.86$	0.0263	8.39	0.4734
MNIST	LIGHTSPLIT-F ($\lambda_{\text{WCC}}=0$)	4	128	8 \times	98.30	0.1628	$\times 0.92$	0.0600	8.26	0.6175
MNIST	LIGHTSPLIT-F ($\lambda_{\text{WCC}}=10^{-2}$)	4	128	8 \times	98.25	0.1656	$\times 0.94$	0.1278	7.81	0.6813
MNIST	LIGHTSPLIT-F ($\lambda_{\text{WCC}}=10^{-1}$)	4	128	8 \times	96.95	0.1656	$\times 0.94$	0.1278	7.81	0.6813
MNIST	LIGHTSPLIT-F ($\lambda_{\text{WCC}}=10^{-1}$)	4	128	8 \times	12.20	0.1656	$\times 0.94$	0.1278	7.81	0.6813
MNIST	LIGHTSPLIT-F ($\lambda_{\text{WCC}}=10^{-1}$)	4	128	8 \times	11.75	0.1656	$\times 0.94$	0.1278	7.81	0.6813
MNIST	LIGHTSPLIT-F ($\lambda_{\text{WCC}}=10^{-1}$)	4	128	8 \times	11.20	0.1656	$\times 0.94$	0.1278	7.81	0.6813
MNIST	LIGHTSPLIT-F ($\lambda_{\text{WCC}}=10^{-1}$)	4	128	8 \times	96.90	0.1656	$\times 0.94$	0.1278	7.81	0.6813
MNIST	LIGHTSPLIT-F ($\lambda_{\text{WCC}}=0$)	4	64	16 \times	98.19	0.1688	$\times 0.95$	0.1178	7.95	0.6463
MNIST	LIGHTSPLIT-F ($\lambda_{\text{WCC}}=10^{-2}$)	4	64	16 \times	98.68	0.1656	$\times 0.94$	0.1278	7.81	0.6813
MNIST	LIGHTSPLIT-F ($\lambda_{\text{WCC}}=10^{-1}$)	4	64	16 \times	11.30	0.1656	$\times 0.94$	0.1278	7.81	0.6813
MNIST	LIGHTSPLIT-F ($\lambda_{\text{WCC}}=0$)	4	32	32 \times	98.58	0.1920	$\times 1.08$	0.1252	7.82	0.6825
MNIST	LIGHTSPLIT-F ($\lambda_{\text{WCC}}=10^{-2}$)	4	32	32 \times	96.97	0.1656	$\times 0.94$	0.1278	7.81	0.6813
MNIST	LIGHTSPLIT-F ($\lambda_{\text{WCC}}=10^{-1}$)	4	32	32 \times	10.15	0.1656	$\times 0.94$	0.1278	7.81	0.6813
Fashion-MNIST	RAW	2	-	-	88.64	0.3010	$\times 1.00$	0.0599	5.26	0.7112
Fashion-MNIST	LEARNED 1×1	2	144	8 \times	87.90	0.3232	$\times 1.07$	0.0086	4.98	0.7102
Fashion-MNIST	LEARNED 1×1	2	72	16 \times	88.60	0.3355	$\times 1.11$	0.0280	4.92	0.7635
Fashion-MNIST	LEARNED 1×1	2	36	32 \times	88.45	0.2790	$\times 0.93$	0.0532	5.56	0.6053
Fashion-MNIST	LIGHTSPLIT-F ($\lambda_{\text{WCC}}=0$)	2	144	8 \times	89.00	0.3243	$\times 1.08$	0.0434	4.90	0.7683
Fashion-MNIST	LIGHTSPLIT-F ($\lambda_{\text{WCC}}=10^{-2}$)	2	144	8 \times	86.05	0.3240	$\times 1.08$	0.0434	4.90	0.7683
Fashion-MNIST	LIGHTSPLIT-F ($\lambda_{\text{WCC}}=10^{-1}$)	2	144	8 \times	84.70	0.3240	$\times 1.08$	0.0434	4.90	0.7683
Fashion-MNIST	LIGHTSPLIT-F ($\lambda_{\text{WCC}}=0$)	2	72	16 \times	87.01	0.3240	$\times 1.08$	0.0434	4.90	0.7683
Fashion-MNIST	LIGHTSPLIT-F ($\lambda_{\text{WCC}}=10^{-2}$)	2	72	16 \times	85.84	0.3240	$\times 1.08$	0.0434	4.90	0.7683
Fashion-MNIST	LIGHTSPLIT-F ($\lambda_{\text{WCC}}=10^{-1}$)	2	72	16 \times	85.75	0.3240	$\times 1.08$	0.0434	4.90	0.7683
Fashion-MNIST	LIGHTSPLIT-F ($\lambda_{\text{WCC}}=0$)	2	36	32 \times	84.03	0.3205	$\times 1.07$	0.0451	4.94	0.7697
Fashion-MNIST	LIGHTSPLIT-F ($\lambda_{\text{WCC}}=10^{-2}$)	2	36	32 \times	85.99	0.3240	$\times 1.08$	0.0434	4.90	0.7683
Fashion-MNIST	LIGHTSPLIT-F ($\lambda_{\text{WCC}}=10^{-1}$)	2	36	32 \times	84.05	0.3240	$\times 1.08$	0.0434	4.90	0.7683
Fashion-MNIST	RAW	4	-	-	88.82	0.3224	$\times 1.00$	0.0450	4.95	0.7451
Fashion-MNIST	LEARNED 1×1	4	128	8 \times	88.35	0.3277	$\times 1.02$	0.0439	5.07	0.6227
Fashion-MNIST	LEARNED 1×1	4	64	16 \times	88.05	0.3493	$\times 1.08$	0.0438	5.05	0.6290
Fashion-MNIST	LEARNED 1×1	4	32	32 \times	88.70	0.3248	$\times 1.01$	0.0094	5.18	0.6519
Fashion-MNIST	LIGHTSPLIT-F ($\lambda_{\text{WCC}}=0$)	4	128	8 \times	89.00	0.3239	$\times 1.00$	0.0434	4.90	0.7683
Fashion-MNIST	LIGHTSPLIT-F ($\lambda_{\text{WCC}}=10^{-2}$)	4	128	8 \times	87.75	0.3240	$\times 1.00$	0.0434	4.90	0.7683
Fashion-MNIST	LIGHTSPLIT-F ($\lambda_{\text{WCC}}=10^{-1}$)	4	128	8 \times	86.10	0.3240	$\times 1.00$	0.0434	4.90	0.7683
Fashion-MNIST	LIGHTSPLIT-F ($\lambda_{\text{WCC}}=10^{-1}$)	4	128	8 \times	84.40	0.3240	$\times 1.00$	0.0434	4.90	0.7683
Fashion-MNIST	LIGHTSPLIT-F ($\lambda_{\text{WCC}}=10^{-1}$)	4	128	8 \times	10.45	0.3240	$\times 1.00$	0.0434	4.90	0.7683
Fashion-MNIST	LIGHTSPLIT-F ($\lambda_{\text{WCC}}=10^{-1}$)	4	128	8 \times	10.45	0.3240	$\times 1.00$	0.0434	4.90	0.7683
Fashion-MNIST	LIGHTSPLIT-F ($\lambda_{\text{WCC}}=10^{-1}$)	4	128	8 \times	84.75	0.3240	$\times 1.00$	0.0434	4.90	0.7683
Fashion-MNIST	LIGHTSPLIT-F ($\lambda_{\text{WCC}}=0$)	4	64	16 \times	87.11	0.3378	$\times 1.05$	0.0436	4.90	0.7702
Fashion-MNIST	LIGHTSPLIT-F ($\lambda_{\text{WCC}}=10^{-2}$)	4	64	16 \times	86.91	0.3240	$\times 1.00$	0.0434	4.90	0.7683
Fashion-MNIST	LIGHTSPLIT-F ($\lambda_{\text{WCC}}=10^{-1}$)	4	64	16 \times	84.45	0.3240	$\times 1.00$	0.0434	4.90	0.7683
Fashion-MNIST	LIGHTSPLIT-F ($\lambda_{\text{WCC}}=0$)	4	32	32 \times	86.96	0.3253	$\times 1.01$	0.0437	4.90	0.7692
Fashion-MNIST	LIGHTSPLIT-F ($\lambda_{\text{WCC}}=10^{-2}$)	4	32	32 \times	84.77	0.3240	$\times 1.00$	0.0434	4.90	0.7683
Fashion-MNIST	LIGHTSPLIT-F ($\lambda_{\text{WCC}}=10^{-1}$)	4	32	32 \times	85.10	0.3240	$\times 1.00$	0.0434	4.90	0.7683

TABLE XVI: FORA reconstruction results on CIFAR-10 across compression ratios $\rho \in \{8\times, 16\times, 32\times\}$ and LIGHTSPLIT-F WCC settings $\lambda_{\text{WCC}} \in \{0, 0.01, 0.1\}$. Both attack heads are reported: *Pseudo decoder* is FORA’s deployable black-box attack (surrogate encoder + adversarial discriminator + decoder trained on auxiliary data, no victim labels) and is the U-shaped SL threat-model attack; *Reference decoder* is a white-box decoder trained directly on the victim’s (h, x) pairs and serves as the leakage ceiling. $\Delta_{\text{Raw}} = \text{LPIPS}_{\text{defence}} / \text{LPIPS}_{\text{Raw}}$ on the reference head; values > 1 mean the cut leaks less than RAW under perfectly-trained inversion. Best defence cell per column highlighted in **bold**.

Method	ρ	λ_{WCC}	Pseudo decoder			Reference decoder (white-box ceiling)			
			SSIM↓	PSNR↓	LPIPS↑	SSIM↓	PSNR↓	LPIPS↑	$\Delta_{\text{Raw}} \uparrow$
RAW	1×	–	–0.42	7.20	0.467	0.940	28.02	0.083	×1.00
LEARNED 1×1	8×	–	0.61	15.61	0.383	0.917	26.27	0.122	×1.5
LEARNED 1×1	16×	–	–0.37	5.51	0.615	0.890	24.87	0.151	×1.8
LEARNED 1×1	32×	–	0.58	15.81	0.365	0.827	22.42	0.214	×2.6
LIGHTSPLIT-F	8×	0	0.04	9.77	0.628	0.440	17.70	0.513	×6.2
LIGHTSPLIT-F	16×	0	0.03	9.39	0.639	0.376	16.89	0.527	×6.3
LIGHTSPLIT-F	32×	0	0.03	9.57	0.636	0.314	16.27	0.551	×6.6
LIGHTSPLIT-F	8×	0.01	0.07	10.38	0.645	0.375	17.11	0.527	×6.3
LIGHTSPLIT-F	16×	0.01	0.02	9.96	0.635	0.323	15.45	0.546	×6.6
LIGHTSPLIT-F	32×	0.01	0.03	9.91	0.640	0.300	16.04	0.560	×6.7
LIGHTSPLIT-F	8×	0.1	0.08	11.57	0.652	0.300	12.01	0.552	×6.7
LIGHTSPLIT-F	16×	0.1	0.07	11.38	0.639	0.276	15.48	0.594	× 7.2
LIGHTSPLIT-F	32×	0.1	0.04	10.27	0.685	0.176	10.09	0.592	×7.1

Notes. The pseudo decoder is trained on the surrogate’s auxiliary distribution rather than the victim’s data, which makes its pixelwise scores (SSIM, PSNR) unstable (negative-SSIM rows reflect surrogate-mismatch artefacts on RAW and LEARNED 1×1 $\rho=16\times$, not “less leakage”). LPIPS, computed in a perceptual feature space, orders the methods consistently.

TABLE XVII: MLP-liftback hidden-dimension ablation for LIGHTSPLIT-L across all four head configurations (the L1H/L2H × SCH/PCH cross). CR=8, IID ($\alpha \rightarrow \infty$), $n=10$ clients, 2000 epochs max, patience 200. Acc = best test accuracy (%); Δ vs. matched RAW baseline for the same (dataset, head). **bold** marks the best hidden width per row.

Dataset	Head	Raw		$h=64$	$h=128$	$h=256$	$h=512$	$h=1024$	$h=2048$	
CIFAR-10	L2H+SCH	87.24	Acc	–	–	85.76	85.91	84.36	83.93	
		Δ	–	–	–1.48	–1.33	–2.88	–3.31		
	L1H+SCH	86.86	Acc	–	–	76.69	78.68	78.07	77.89	
		Δ	–	–	–10.17	–8.18	–8.79	–8.97		
	L2H+PCH	78.31	Acc	–	–	70.34	70.59	70.90	70.70	
		Δ	–	–	–7.97	–7.72	–7.41	–7.61		
	L1H+PCH	81.28	Acc	–	–	71.82	73.00	71.77	72.25	
		Δ	–	–	–9.46	–8.28	–9.51	–9.03		
	CIFAR-100	L2H+SCH	59.47	Acc	–	–	52.23	54.10	54.38	55.34
			Δ	–	–	–7.24	–5.37	–5.09	–4.13	
		L1H+SCH	59.56	Acc	–	–	44.45	44.82	44.82	45.52
			Δ	–	–	–15.11	–14.74	–14.74	–14.04	
L2H+PCH		47.09	Acc	–	–	38.24	38.15	38.44	37.58	
		Δ	–	–	–8.85	–8.94	–8.65	–9.51		
L1H+PCH		49.95	Acc	–	–	39.72	40.96	41.04	40.20	
		Δ	–	–	–10.23	–8.99	–8.91	–9.75		
FashionMNIST		L2H+SCH	91.91	Acc	90.91	91.22	91.16	91.21	91.16	–
			Δ	–1.00	–0.69	–0.75	–0.70	–0.75	–	
		L1H+SCH	91.75	Acc	90.29	90.14	90.10	90.29	90.09	–
			Δ	–1.46	–1.61	–1.65	–1.46	–1.66	–	
	L2H+PCH	88.75	Acc	85.34	84.79	85.58	85.98	86.00	–	
		Δ	–3.41	–3.96	–3.17	–2.77	–2.75	–		
	L1H+PCH	88.81	Acc	84.99	84.56	84.85	84.36	84.25	–	
		Δ	–3.82	–4.25	–3.96	–4.45	–4.56	–		
	GTSRB	L2H+SCH	98.82	Acc	95.67	95.88	95.59	95.49	95.27	–
			Δ	–3.15	–2.94	–3.23	–3.33	–3.55	–	
		L1H+SCH	98.05	Acc	89.11	89.35	89.92	89.63	89.15	–
			Δ	–8.94	–8.70	–8.13	–8.42	–8.90	–	
L2H+PCH		97.52	Acc	93.52	93.00	92.76	92.68	92.72	–	
		Δ	–4.00	–4.52	–4.77	–4.84	–4.80	–		
L1H+PCH		96.12	Acc	87.36	86.96	86.60	86.06	87.60	–	
		Δ	–8.76	–9.16	–9.52	–10.06	–8.52	–		